Vertical Moist Thermodynamic Structure and Spatial–Temporal Evolution of the MJO in AIRS Observations

BAIJUN TIAN

Division of Geological and Planetary Sciences, California Institute of Technology, Pasadena, California

DUANE E. WALISER, ERIC J. FETZER, AND BJORN H. LAMBRIGTSEN

Jet Propulsion Laboratory, California Institute of Technology, Pasadena, California

YUK L. YUNG

Division of Geological and Planetary Sciences, California Institute of Technology, Pasadena, California

BIN WANG

Department of Meteorology, and International Pacific Research Center, University of Hawaii at Manoa, Honolulu, Hawaii

(Manuscript received 15 November 2005, in final form 3 March 2006)

ABSTRACT

The atmospheric moisture and temperature profiles from the Atmospheric Infrared Sounder (AIRS)/Advanced Microwave Sounding Unit on the NASA *Aqua* mission, in combination with the precipitation from the Tropical Rainfall Measuring Mission (TRMM), are employed to study the vertical moist thermodynamic structure and spatial–temporal evolution of the Madden–Julian oscillation (MJO). The AIRS data indicate that, in the Indian Ocean and western Pacific, the temperature anomaly exhibits a trimodal vertical structure: a warm (cold) anomaly in the free troposphere (800–250 hPa) and a cold (warm) anomaly near the tropopause (above 250 hPa) and in the lower troposphere (below 800 hPa) associated with enhanced (suppressed) convection. The AIRS moisture anomaly also shows markedly different vertical structures as a function of longitude and the strength of convection anomaly. Most significantly, the AIRS data demonstrate that, over the Indian Ocean and western Pacific, the enhanced (suppressed) convection is generally preceded in both time and space by a low-level warm and moist (cold and dry) anomaly and followed by a low-level cold and dry (warm and moist) anomaly.

The MJO vertical moist thermodynamic structure from the AIRS data is in general agreement, particularly in the free troposphere, with previous studies based on global reanalysis and limited radiosonde data. However, major differences in the lower-troposphere moisture and temperature structure between the AIRS observations and the NCEP reanalysis are found over the Indian and Pacific Oceans, where there are very few conventional data to constrain the reanalysis. Specifically, the anomalous lower-troposphere temperature structure is much less well defined in NCEP than in AIRS for the western Pacific, and even has the opposite sign anomalies compared to AIRS relative to the wet/dry phase of the MJO in the Indian Ocean. Moreover, there are well-defined eastward-tilting variations of moisture with height in AIRS over the central and eastern Pacific that are less well defined, and in some cases absent, in NCEP. In addition, the correlation between MJO-related midtropospheric water vapor anomalies and TRMM precipitation anomalies is considerably more robust in AIRS than in NCEP, especially over the Indian Ocean. Overall, the AIRS results are quite consistent with those predicted by the frictional Kelvin–Rossby wave/conditional instability of the second kind (CISK) theory for the MJO.

Corresponding author address: Dr. Baijun Tian, Jet Propulsion Laboratory, California Institute of Technology, M/S 183-501, 4800 Oak Grove Dr., Pasadena, CA 91109.
E-mail: baijun.tian@jpl.nasa.gov

1. Introduction

The Madden–Julian oscillation (MJO; Madden and Julian 1971, 1972) is the dominant component of the intraseasonal (30–90 day) variability in the tropical atmosphere. It is characterized by a slow eastward propagation ($\sim$5 m s^{-1}) of deep convection and large-scale circulation anomalies mainly in the equatorial Indian Ocean and western Pacific (Madden and Julian 2005; Wang 2005; Zhang 2005). Since its discovery, the MJO has continued to be a topic of significant interest because of its complex nature and profound influence on the global weather and climate at all time scales. Unfortunately, we are still facing great difficulties of accurately simulating and predicting the MJO using even the most sophisticated global climate and weather forecast models (e.g., Slingo et al. 1996, 2005; Waliser et al. 2003b; Waliser 2006). Furthermore, a comprehensive theory for the MJO that accounts for all the fundamental characteristics of the MJO, such as initiation in the western Indian Ocean, slow eastward propagation in the Indian Ocean and western Pacific, and intraseasonal time scale, has proven elusive (see Wang 2005 for a detailed review). It is fair to say that understanding, modeling, and predicting the MJO still remains a challenge for tropical atmospheric scientists and oceanographers (see Lau and Waliser 2005 and Zhang 2005 for detailed summaries).

Observational analyses of the large-scale three-dimensional structure and spatial–temporal evolution of the MJO have proven valuable in addressing this challenge. Studies to date have made the most of the available, yet sparse, radiosonde data (e.g., Hendon and Liebmann 1990; Lin and Johnson 1996; Kemball-Cook and Weare 2001; Kiladis et al. 2005), the comprehensive, yet model-dependent, reanalysis products, such as the National Centers for Environmental Prediction–National Center for Atmospheric Research (NCEP–NCAR) reanalysis (Kalnay et al 1996) and the European Centre for Medium-Range Weather Forecasts (ECMWF) reanalysis (Gibson et al. 1997; e.g., Rui and Wang 1990; Hendon and Salby 1994; Jones and Weare 1996; Maloney and Hartmann 1998; Sperber 2003; Seo and Kim 2003; Hsu and Lee 2005; Kiladis et al. 2005), and in a few cases vertically resolving satellite data (e.g., Bantzer and Wallace 1996; Myers and Waliser 2003). In general these studies have characterized a number of important properties of the MJO. For example, MJO convection is preceded by low-level mass convergence, upward motion, warming, and moistening. Furthermore, free tropospheric warming and moistening coincide with MJO convection. While these studies have been instrumental in helping to formulate our conceptual and theoretical understanding of the MJO, they are still subject to a number of limitations and uncertainties. For example, the radiosonde analyses are limited to the fringes of the Indian Ocean but do not include the equatorial region where the most important components of the MJO thermodynamic activity occur. The excellent vertical radiosonde profiles from field experiments like the Tropical Ocean Global Atmosphere (TOGA) Coupled Ocean–Atmosphere Experiment (COARE) have significantly advanced our understanding of the MJO (Lin and Johnson 1996); however, the spatial and temporal coverage of the TOGA COARE radiosonde data is limited. Similarly, because of the lack of observations, there are virtually no radiosonde analyses of MJO-driven thermodynamic variability in the central and eastern Pacific Ocean. Moreover, the lack of radiosonde data in these regions makes results based on reanalysis efforts more suspect as the data in these regions is more strongly determined by the model component of the reanalysis. Finally, while there have been some satellite data sources available for MJO analysis (e.g., Bantzer and Wallace 1996; Myers and Waliser 2003) as well as for inclusion into the reanalyses, the vertical resolution, particularly in the lower troposphere where it is most needed, is rather low ($\sim$3–4 km). Thus, the vertical moist thermodynamic structure of the MJO requires continued examination based on improved observations.

The Atmospheric Infrared Sounder (AIRS)/Advanced Microwave Sounding Unit (AMSU) is a new satellite-based sounding system on the National Aeronautics and Space Administration (NASA) *Aqua* mission, and is the most advanced temperature and humidity sounding system ever deployed (Parkinson 2003). Through multispectral coverage in infrared and microwave channels, the AIRS/AMSU system obtains vertical profiles of atmospheric temperature and water vapor with vertical resolution of 1–2 km, horizontal resolution of 45 km, temporal resolution of twice daily, radiosonde accuracy, global coverage, and for cloud cover up to about 70%. Thus, the AIRS data provide an unprecedented opportunity to examine the MJO three-dimensional structure. In this study, we seek to exploit these high-resolution soundings to characterize the vertical moist thermodynamic structure and spatial–temporal evolution of the MJO. In addition, by comparing results from AIRS and the NCEP reanalysis, an extensively used reanalysis for MJO studies, we hope to illustrate areas where confidence can be ascribed to the reanalyses as well as highlight areas for where caution might be warranted.

The outline for the rest of this paper is as follows:

The data and methodology are introduced in section 2. Section 3 presents the main observational results of this study followed by a comparison with those obtained using NCEP in section 4. Section 5 summarizes the major findings of this study and discusses the implications of these observational results to MJO theory.

2. Data and methodology

a. AIRS

The AIRS experiment includes the AIRS, AMSU, and the Humidity Sounder for Brazil (HSB) instruments but HSB malfunctioned after launch. This study uses retrievals based only on AIRS and AMSU. The AIRS/AMSU sounding system, which is included on the NASA *Aqua* platform, has been operational since 1 September 2002. The two instruments are each cross-track scanning nadir sounders that are coaligned and have a swath roughly 1650 km wide. The AIRS instrument is a 2378-channel grating spectrometer measuring infrared radiance at wavelengths in the range 3.7–15.4 μm. The horizontal resolution is about 13.5 km at nadir (Aumann et al. 2003). These wavelengths are sensitive to clouds, surface properties, minor gases, and profiles of temperature and water vapor. AMSU is a 15-channel microwave radiometer with a horizontal resolution of about 45 km at nadir. Twelve AMSU channels are sensitive to temperature, with the other three channels used for water vapor measurement and precipitation detection.

The retrieval method for AIRS geophysical quantities uses an iterative, least squares physical inversion of clear column radiances, obtained from a combination of infrared and microwave observations following the approach of Chahine (1968, 1977). The AIRS retrieval algorithm is described by Susskind et al. (2003), and includes forward radiative models for calculating infrared (Strow et al. 2003) and microwave spectra (Rosenkranz 2003). The retrieval methodology uses a set of a single AMSU microwave spectrum and nine associated AIRS infrared spectra. AIRS obtains 324 000 profile estimates daily. The horizontal resolution of profile quantities is 45 km, the same as AMSU observations. While the true vertical resolution of AIRS is not known, simulations indicate resolution of about 1 km for temperature and 2 km for water vapor in the lower and middle troposphere (Susskind et al. 2003). Those numbers pertain to individual profiles, while the results shown here are based on composites over many thousands of soundings. The composite profiles can be expected to have better vertical resolution.

The resulting AIRS profiles have specified tropospheric uncertainties of 1 K in 1-km layers for temperature, and 15% of mean specific humidity in 2-km layers for water vapor. These uncertainties have been confirmed empirically through validation studies for a wide range of conditions using operational radiosondes (Divakarla et al. 2006), and best-estimate atmospheric conditions from a suite of in situ observations (Tobin et al. 2006). The Tobin et al. analysis includes comparisons with AIRS-dedicated radiosondes at Nauru Island in the equatorial Pacific Ocean (0.54°S, 166.93°E), where AIRS retrievals exceed the measurement specification for temperature and water vapor described above. Gettelman et al. (2004) showed that AIRS retrievals in the moist Tropics have uncertainties in water vapor of 20% or less in the upper troposphere below 150-hPa pressure level, and temperature uncertainties of ~1K into the stratosphere. The AIRS water retrievals have uncertainties of 30%–50% over land versus 20% over water. In radiosonde comparisons over nondesert land and water regions, these uncertainties are dominated by a random component (Tobin et al. 2006; Divakarla et al. 2006). These random uncertainties will be reduced by the averaging effect of the composing technique used in this study. Our studies indicate desert regions have spurious wet biases in AIRS retrievals, but these regions lie outside the limits of this study. Finally, sensitivity studies indicate that land-induced uncertainties do not affect the conclusions of our study because the MJO is most active in the equatorial Indian and western Pacific Oceans.

The primary data in this study are the daily (count-weighted average of the ascending and descending modes) AIRS level 3 v4.0.8.0 atmospheric moisture and temperature profiles from 1 September 2002 to 26 January 2005. The data have a horizontal resolution of 1° latitude × 1° longitude, and the vertical grid is based on the World Meteorological Organization (WMO) standard pressure levels from 1000 to 1 hPa for temperature and layers from 1000 to 100 hPa for water vapor.

The AIRS level 3 data include only those retrievals utilizing both infrared (AIRS) and microwave (AMSU) observations, designated full retrievals. The validation studies described above have also concentrated on AIRS full retrievals. The AIRS full retrieval yield is a strong function of cloud amount, dropping to zero for effective cloud fraction (the product of true fraction and infrared emissivity) greater than about 70%. This yield can vary with time and location, and be as small as 15% in some regions studied here. Yields typically range between 30% and 80%, with slight day/night differences presumably due to diurnal cycles in cloudiness. Fetzer et al. (2006) show that AIRS total water vapor is unbiased in regions of deep convection, even when

AIRS yields are small. This implies that the AIRS lower tropospheric humidity, at least, is also unbiased.

b. Other data sources

Tropical Rainfall Measuring Mission (TRMM) adjusted merged-infrared precipitation (3B42) from 1 January 1998 to 4 February 2005 was used to identify MJO events. The TRMM 3B42 rainfall is on a 3-h temporal resolution and a 0.25° × 0.25° spatial resolution in a global belt extending from 50°S to 50°N. In the following discussion, rainfall is used as a proxy for MJO convection. To compare the MJO vertical structure based on AIRS with that from traditional global reanalysis products, the daily NCEP reanalysis and the NCEP–Department of Energy (DOE) reanalysis (Kanamitsu et al. 2002; NCEP2 for simplicity) at the same period as AIRS were also employed. The vertical resolution of NCEP temperature profile is the WMO standard pressure levels from 1000 to 10 hPa and from 1000 to 300 hPa for water vapor. The latitude–longitude resolution of the NCEP reanalysis is 2.5° × 2.5°. For validation purposes, the contemporaneous daily NCEP quality-controlled radiosonde data at Truk, Micronesia (7.47°S, 151.85°E), were also utilized.

c. Compositing procedure

Because of the limited number of MJO events in this study, pentad data were used for the MJO analysis instead of daily data in order to give adequate samples on a given map. The data from TRMM, AIRS, NCEP, and radiosonde were first binned into 5-day average (i.e., pentad) values. Then, the annual cycle was calculated based on the pentad data and smoothed with a 30-day running mean. Next, pentad anomalies were obtained by removing the annual cycle from the pentad data. Last, MJO anomalies (or just anomalies for simplicity) were isolated through the difference between the 15-day and 45-day running means of the pentad anomalies. A time–longitude diagram of TRMM rainfall anomalies along the equator (not shown) indicates that a number of MJO events (~10–15) are evident during the AIRS data period. To obtain a representative MJO vertical structure and spatial–temporal evolution, MJO events were chosen based on an extended empirical orthogonal function (EEOF) analysis (Weare and Nasstrom 1982), using a temporal lag of 11 pentads (from −5 to +5 pentads), of the TRMM rainfall anomalies from Northern Hemisphere (NH) wintertime (November–April) and the region 30°N–30°S and 30°E–150°W. This region, that is, mainly equatorial Indian Ocean and western Pacific, is the active geographic region of the classic eastward propagating MJO with a peak season in the NH wintertime (e.g., Madden 1986; Wang and Rui 1990a; Jones et al. 2004; Zhang and Dong 2004).

The spatial–temporal pattern for the first EEOF mode, explaining about 6% variance, is shown in Fig. 1 and depicts the bulk characteristics of a typical MJO cycle in terms of rainfall anomaly. MJO convection first develops in the western Indian Ocean, then slowly propagates eastward in the Indian Ocean and western Pacific, and finally disappears in the central Pacific, consistent with previous studies, such as Wang and Rui (1990a) and Hendon and Salby (1994). In this depiction, the MJO appears to oscillate with a period of about 40 days. Also consistent with Hsu and Lee (2005), the eastward propagation of MJO convection is typically not continuous and occurs mainly in two regions: the Indian Ocean (60°–110°E) and the western Pacific warm pool (135°E–170°W). The Maritime Continent where the eastward propagation is very weak separates these two regions.

Figure 2 shows the amplitude pentad time series of the first EEOF mode of the NH wintertime TRMM rainfall anomaly for the AIRS period. MJO events are selected for compositing if their peak time series amplitude is greater than +1 standard deviation (e.g., Waliser et al. 2003a), Based on this simple criterion, eight MJO events were selected for the AIRS data period, as indicated by eight crosses in Fig. 2. For each selected MJO event, the corresponding 11-pentad rainfall, temperature, and water vapor anomalies were extracted for each dataset (TRMM, AIRS, NCEP, and radiosonde). A composite MJO cycle (11 pentads) of the anomalies was then obtained by averaging the eight selected MJO events. Sensitivity study based on a longer time period of NCEP data indicates that the MJO structure based on the current eight MJO events should be significant and useful to report at this stage.

3. Observed MJO vertical structure from AIRS

a. MJO vertical thermodynamic structure

Figure 3 shows the pressure–longitude cross sections of temperature anomaly for the composite MJO cycle. For simplicity, only lags from −3 to +3 pentads of the MJO cycle are shown. Please note that the MJO structure of lag +4 pentads is very similar to that of lag −4 and −3 pentads. In addition, the line plots overlaid on the contour diagrams are the corresponding MJO-related TRMM rainfall anomalies. Note that the magnitude of the composite temperature anomalies ranges up to about ±0.4 K. However, inspection of the individual events shows that they range up to about ±1.5 K

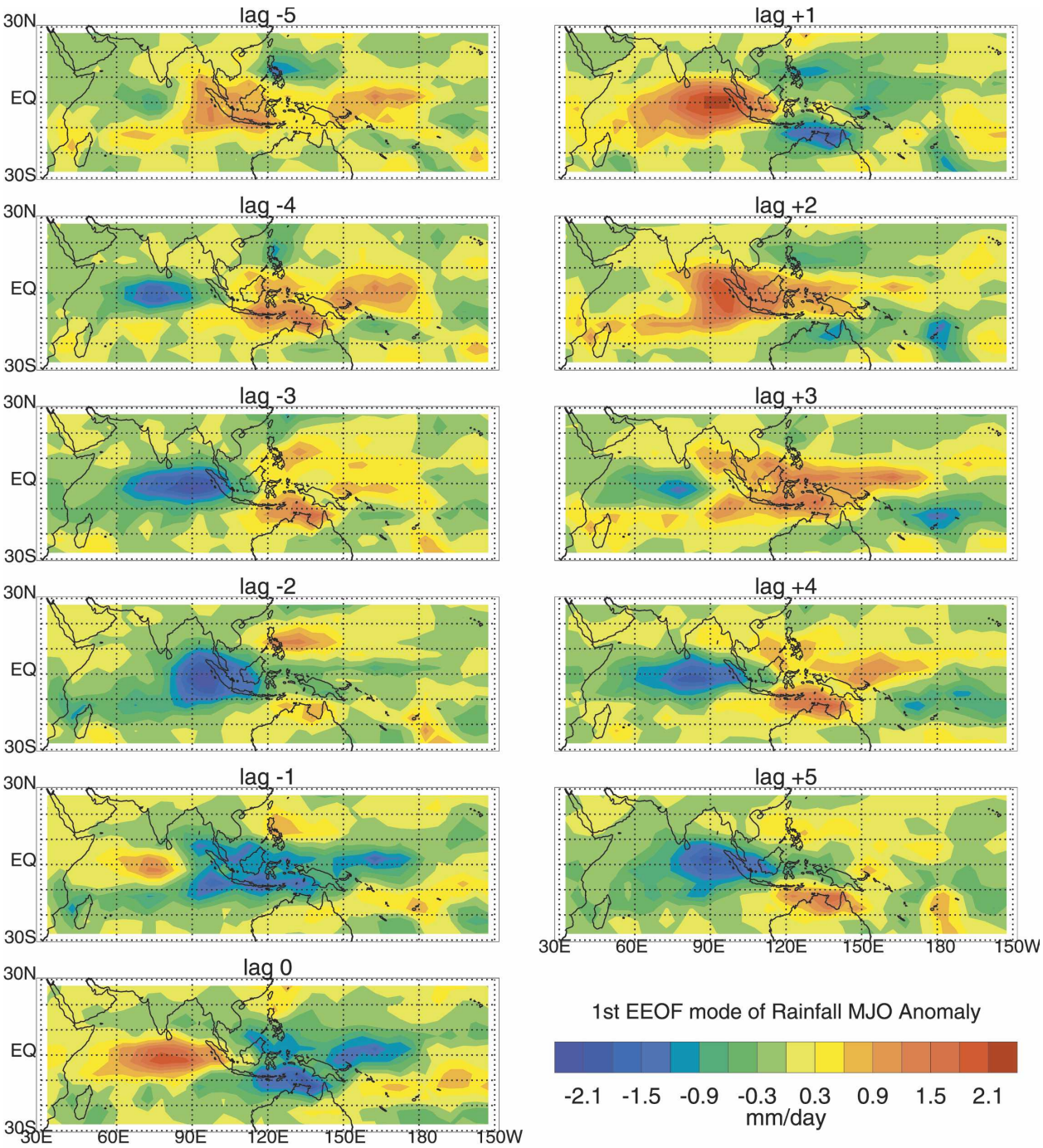

FIG. 1. Spatial–temporal pattern for the first EEOF mode of TRMM rainfall anomaly from NH wintertime (November–April) and the region 30°N–30°S and 30°E–150°W. The unit for the lag is pentad. The color red denotes positive rainfall anomalies, i.e., enhanced convection, while the color blue indicates negative rainfall anomalies, i.e., suppressed convection.

but the compositing procedure reduces the signal amplitude.

In the Indian Ocean and western Pacific, where MJO convection is active, the temperature anomaly shows a trimodal vertical structure with roughly three layers: lower troposphere (below 800 hPa), free troposphere (800–250 hPa), and tropopause region (above 250 hPa). Near the tropopause (above 250 hPa), a cold (warm) anomaly (~0.2 K) is generally found over the region of enhanced (suppressed) convection with a maximum in

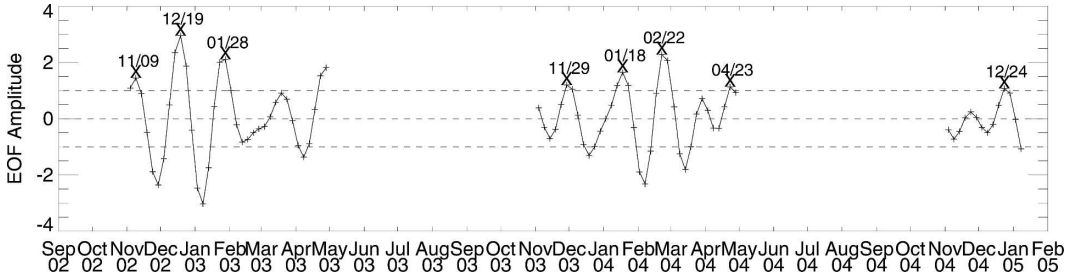

FIG. 2. Amplitude pentad time series for the first EEOF mode of TRMM rainfall anomaly from NH wintertime (November–April) and the region 30°N–30°S and 30°E–150°W.

the lower stratosphere, indicating that deep convection—at least as organized by the MJO—tends to locally cool the tropopause region (see also Lin and Johnson 1996; Sherwood et al. 2003; Kiladis et al. 2005; Kim and Dessler 2004). The tropopause temperature anomaly exhibits a structure tilting upward from west to east and appears to be part of the global-scale temperature anomaly signals originating from the upper troposphere over the western Pacific, which is a well-documented feature of the MJO (Eguchi and Shiotani 2004; Kiladis et al. 2005). This tilted structure appears to be a manifestation of the higher-order of vertical modes that results from a large change in the stratification in the tropopause region (Wang and Chen 1989).

In the free troposphere (800–250 hPa) in Fig. 3, a warm (cold) anomaly (~0.4 K) is collocated with enhanced (suppressed) convection with a maximum in the upper or middle troposphere, suggesting that deep convection tends to locally warm the free troposphere (Hendon and Liebmann 1990; Lin and Johnson 1996; Kemball-Cook and Weare 2001; Sherwood et al. 2003; Kiladis et al. 2005). In the Indian Ocean, the extrema tend to be in the middle troposphere (500 hPa), while it tends to be in the upper troposphere (350 hPa) over the western Pacific and shifts slightly upward over the central Pacific. In the lower troposphere (below 800 hPa) in Fig. 3, on the other hand, a cold (warm) anomaly (~0.2 K) is generally found under the region of enhanced (suppressed) convection with a maximum near the surface, implying that deep convection tends to locally cool the lower troposphere and the surface (Hendon and Liebmann 1990; Lin and Johnson 1996; Kemball-Cook and Weare 2001; Sherwood et al. 2003; Kiladis et al. 2005). Note that Kiladis et al. (2005) found higher vertical mode tropospheric temperature structures over the Indian Ocean (their Figs. 8a,b) based on the radiosonde data, somewhat different than the structures shown here. This could be due to a number of factors, such as sampling, the location of these stations south of the equator, and seasonality.

Over the Western Hemisphere (i.e., east of the date line), where MJO convection is weak, significant temperature anomalies are also found in the free troposphere and the tropopause region, which have the same sign as those over the western Pacific. In these regions, the temperature anomaly tends to have a bimodal vertical structure (a difference between troposphere and stratosphere) compared to the trimodal structure to the west.

To examine the horizontal structure of the temperature anomalies in the three layers above and their relationships with the convection anomaly, maps of temperature anomalies representing the tropopause region, the free troposphere, and the lower troposphere are shown in Figs. 4, 5, and 6, respectively. In addition, contour lines of ± 1 mm day^{-1} rainfall anomaly are also shown in the maps. The eastward propagation of warm (cold) anomalies in the free troposphere (Fig. 5) and cold (warm) anomalies in the tropopause region (Fig. 4) and the lower troposphere (Fig. 6) are coincident with the eastward propagation of the enhanced (suppressed) convection anomaly. It is also interesting to note that significant upper tropospheric and tropopause temperature anomalies over the central and eastern Pacific are equatorially confined (Figs. 3, 4, and 5), implying an equatorial Kelvin wave response to the enhanced (suppressed) convection in the western Pacific (Gill 1980). Furthermore, significant off-equatorial cold (warm) anomalies in 100 hPa (Fig. 4) and warm (cold) anomalies in 400 hPa (Fig. 5) are found to the west of the enhanced (suppressed) convection, suggesting an equatorial Rossby wave response to the enhanced (suppressed) convection (Gill 1980). This horizontal structure of the MJO temperature anomaly from AIRS is consistent with the previous studies of Hendon and Salby (1994) and Bantzer and Wallace (1996) based on the coarse-resolution Microwave Sounding Unit (MSU) temperature data. However, the magnitude from AIRS is much larger than the MSU estimate from Bantzer and Wallace (1996) due presumably to the resolution difference.

A lower-troposphere preconditioning temperature

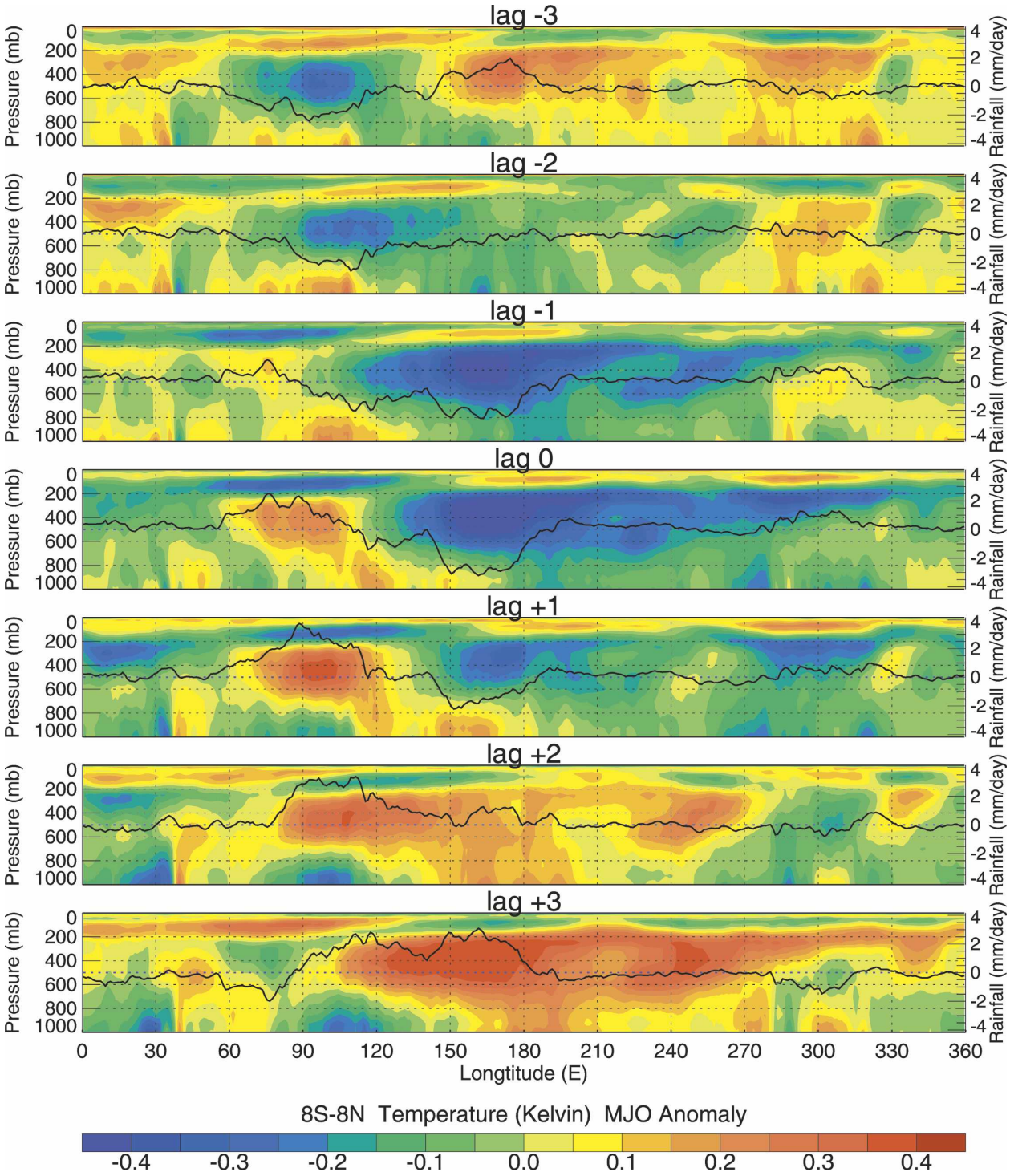

FIG. 3. Pressure–longitude cross sections of temperature anomaly (K) for the composite MJO cycle based on AIRS data. For simplicity, only lags from −3 to +3 pentads of the MJO cycle are shown. The color red denotes positive temperature anomalies, i.e., warming, while the color blue indicates negative temperature anomalies, i.e., cooling. The superimposed solid black line denotes the associated TRMM rainfall anomaly at the AIRS spatial resolution (1° × 1°). The anomalies are averaged from 8°S to 8°N.

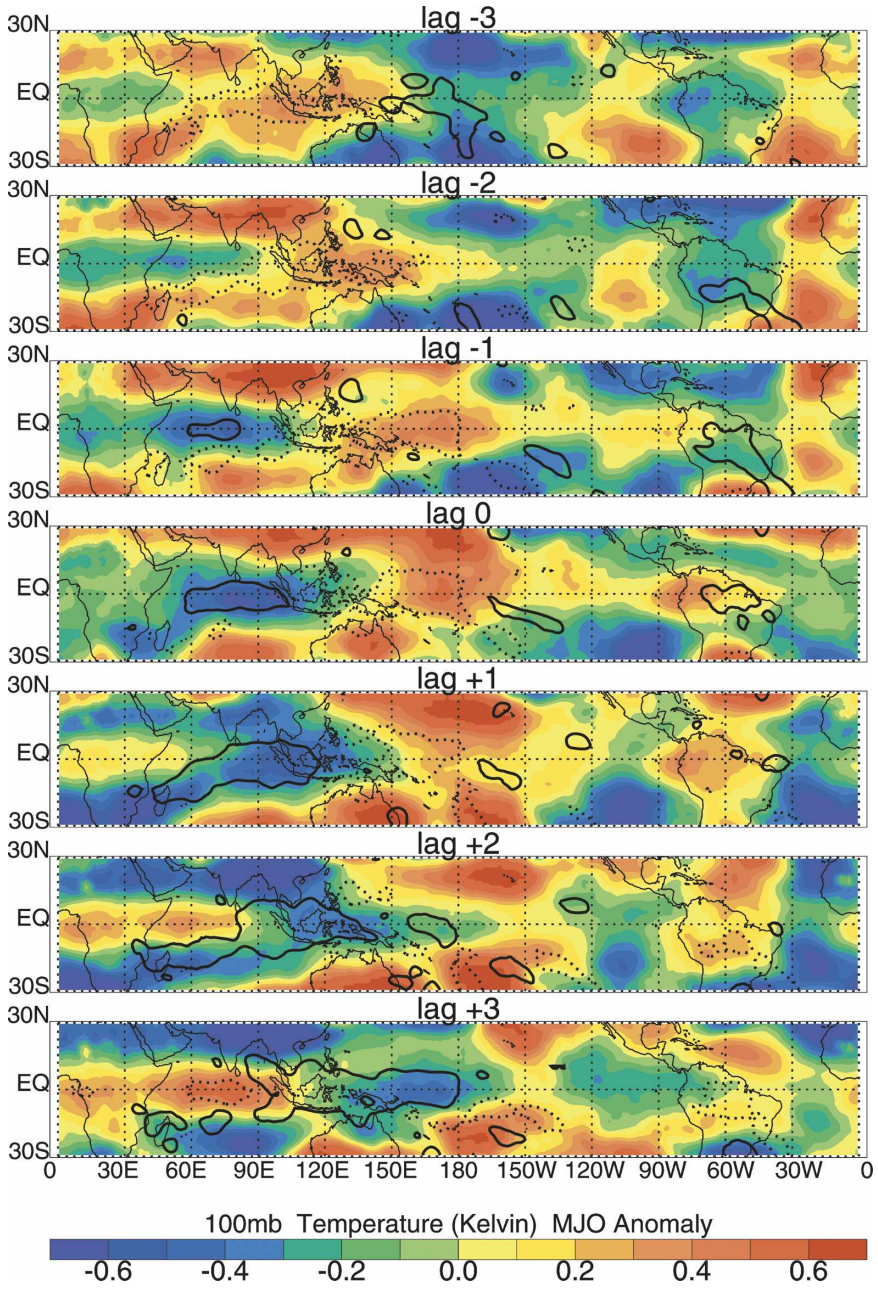

FIG. 4. Spatial pattern of temperature anomaly (K) at 100 hPa for the composite MJO cycle based on AIRS. The superimposed solid black line denotes the TRMM rainfall anomaly of 1 mm day^{-1}, while the dashed black line indicates the TRMM rainfall anomaly of -1 mm day^{-1}.

anomaly associated with the development of the MJO convection anomaly is very evident in the AIRS data for both the Indian and western Pacific Oceans. Specifically, the enhanced (suppressed) convection is generally preceded by a lower-tropospheric warm (cold) anomaly and followed by a lower-tropospheric cold (warm) anomaly in both time and space (Figs. 3 and 6). For example, at lag +1 pentads, enhanced convection and associated free-tropospheric warm anomaly are located over the Indian Ocean (~60°–120°E), while suppressed convection and associated free-tropospheric cold anomaly are centered over the western Pacific (~130°E–170°W). However, a lower-tropospheric cold anomaly is seen over the Indian Ocean, while a lower-tropospheric warm anomaly is found over the western Pacific. The lower-tropospheric warm anomaly over the

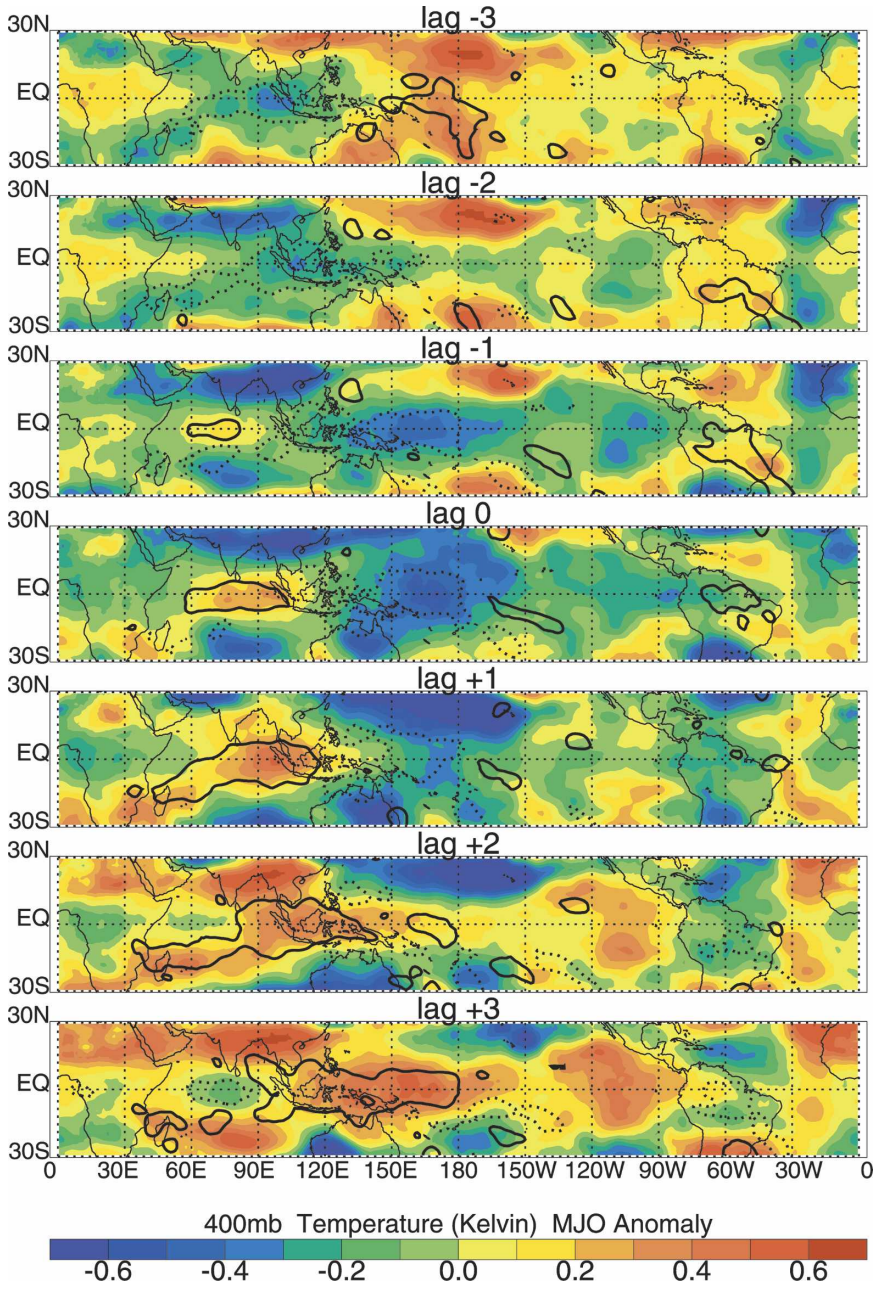

FIG. 5. As in Fig. 4 but for temperature anomaly (K) at 400 hPa.

western Pacific leads (~60° longitude east) the enhanced convection over the Indian Ocean, and the latter is followed (under and to the west) by the lower-tropospheric cold anomaly over the Indian Ocean. Similarly, considering a specific location, such as 90°E at the equator, the MJO convection at lag +1 pentads is preceded (~4 pentads ahead) by a lower-tropospheric warm anomaly (lag −3 or +4 pentads) and followed immediately by a lower-tropospheric cold anomaly. Note that the eastward propagating MJO convection implies a consistent lead/lag relationship in time and space. Please note that the MJO vertical temperature structure observed by AIRS is in general agreement with previous studies based on limited radiosonde data, such as Hendon and Liebmann (1990), Lin and Johnson (1996), Kemball-Cook and Weare (2001), and Kiladis et al. (2005) as discussed in the introduction.

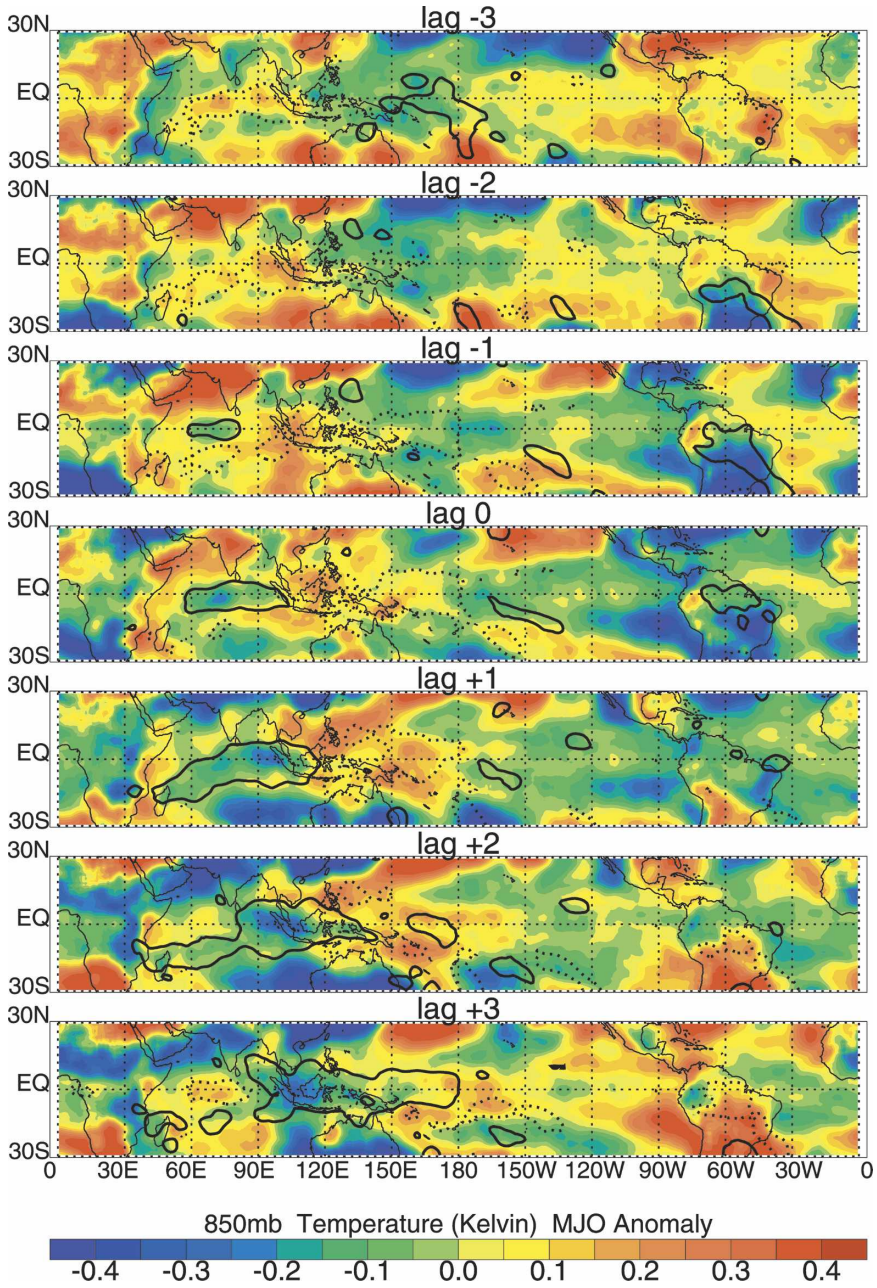

FIG. 6. As in Fig. 4 but for temperature anomaly (K) at 850 hPa.

b. MJO vertical moisture structure

Diagrams similar to Figs. 3, 4, 5, and 6 but for specific humidity are shown in Figs. 7, 8, and 9, respectively. In this case, the horizontal maps are for 648 hPa (Fig. 8, representing middle and lower troposphere from 547 to 886 hPa), and 961 hPa (Fig. 9, representing surface layer).

The moisture anomaly shows markedly different vertical structures as a function of longitude, similar to the findings by Myers and Waliser (2003), and also as a function of the strength of the convection anomaly. In the regions of strongly enhanced (suppressed) convection in the Indian Ocean and western Pacific, moist (dry) anomalies ($\sim$0.3 g kg^{-1}) are generally found throughout the atmospheric column above 925 hPa with a maximum in the middle or lower troposphere. This is consistent with the traditional view that deep convection serves to locally moisten the upper troposphere (Held and Soden 2000; Tian et al. 2004).

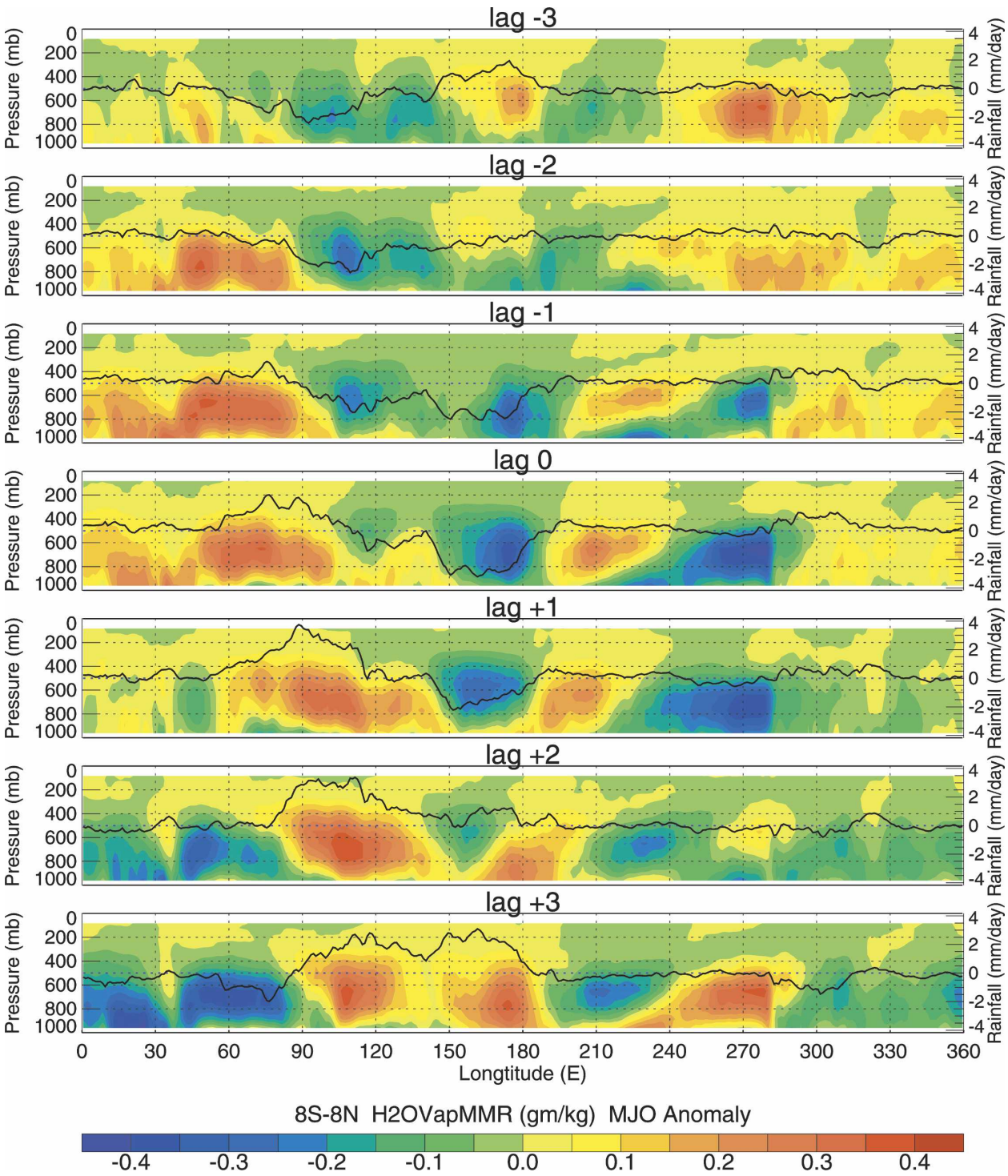

FIG. 7. As in Fig. 3 but for specific humidity anomaly (g kg^{-1}). The color red denotes positive moisture anomalies, i.e., moistening, while the color blue indicates negative moisture anomalies, i.e., drying.

Figure 7 also suggests that AIRS can sense free tropospheric moist (dry) anomalies reaching up to the lower stratosphere (83 hPa), and that deep convection tends to moisten the stratosphere and may play an important role in controlling the stratospheric water vapor (Sherwood and Dessler 2000). Near the surface (961 hPa), weak dry (moist) anomalies (~0.1 g kg^{-1}) are generally found under the regions of the strongly enhanced (sup-

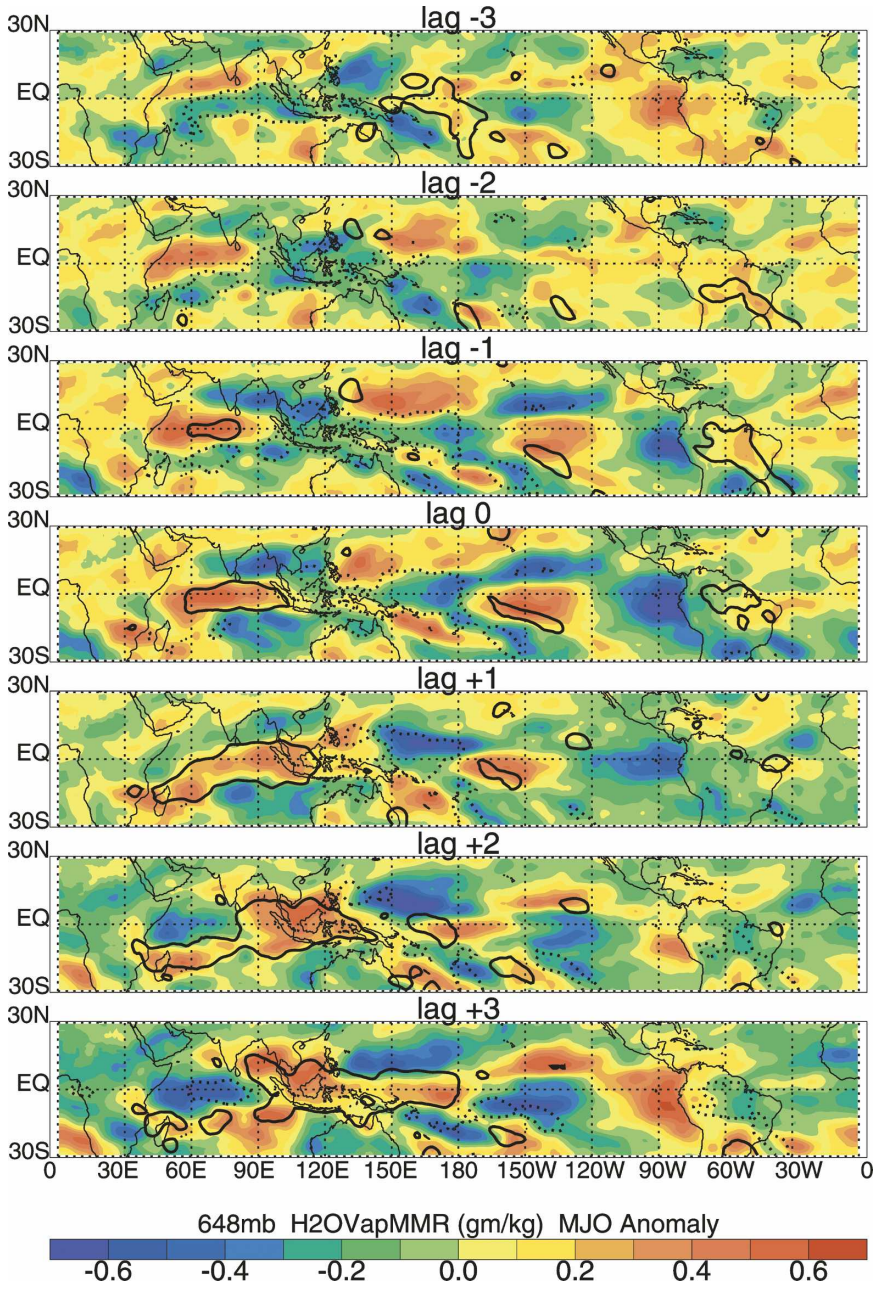

FIG. 8. As in Fig. 4 but for specific humidity anomaly (g kg^{-1}) at 648 hPa.

pressed) convection. In the regions of weakly enhanced (suppressed) convection over the Indian Ocean and western Pacific, there exists a bimodal structure, with moist (dry) (~0.1 g kg^{-1}) anomalies in the upper troposphere (above 500 hPa) and dry (moist) (~0.3 g kg^{-1}) anomalies in the middle and lower troposphere (below 500 hPa). In addition, the eastward propagation of the upper tropospheric moist (dry) anomaly and lower tropospheric and near-surface dry (moist) anomaly is apparent along the eastward propagation of the enhanced (suppressed) convection anomaly (Figs. 7, 8, and 9). The AIRS-observed MJO vertical moisture structure over the Indian Ocean and western Pacific is consistent with that observed by Kemball-Cook and Weare (2001) based on radiosonde data.

Over the Western Hemisphere, where MJO convection is small, the water vapor anomalies are surprisingly large (~0.4 g kg^{-1}), especially over the eastern Pacific, as noted by Myers and Waliser (2003). In the eastern Pacific, large moisture variations are mainly confined to

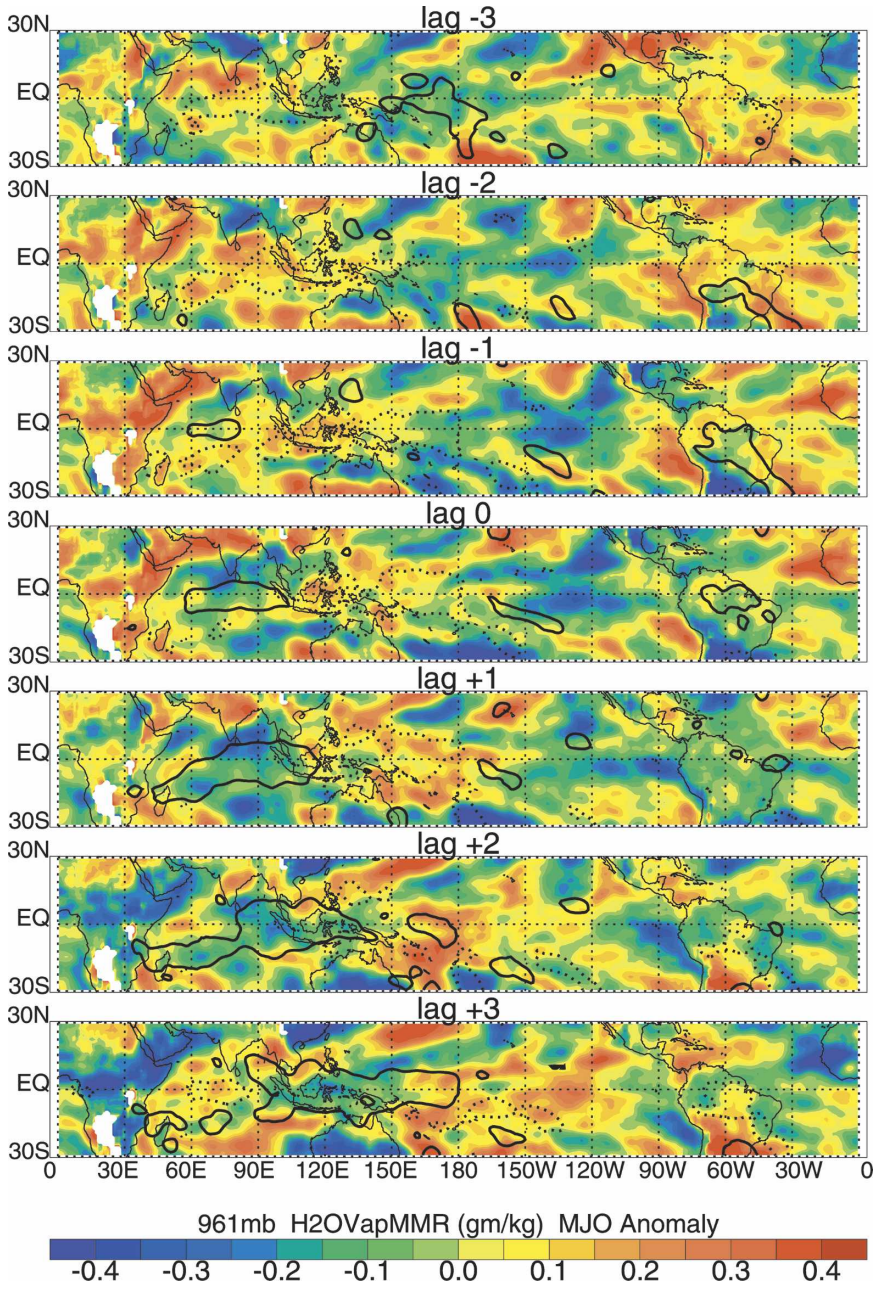

FIG. 9. As in Fig. 4 but for specific humidity anomaly (g kg^{-1}) at 961 hPa.

the lower troposphere (below 500 hPa), with small out-of-phase variations above. It should also be mentioned that AIRS reveals a westward tilt of moisture anomaly with height over the Indian Ocean (Fig. 7), which has been extensively documented by previous studies, such as Sperber (2003), Seo and Kim (2003), and Kiladis et al. (2005) based on NCEP or ECMWF and by Myers and Waliser (2003) based on the Television Infrared Observation Satellite (TIROS) Operational Vertical Sounder (TOVS). However, over the western Pacific, this vertical tilt seems disappear and develop into an eastward tilt of moisture anomaly with height over the central Pacific Ocean (Myers and Waliser 2003).

Most importantly, similar to temperature anomaly, there is also a clear preconditioning lower tropospheric water vapor anomaly for the convection anomaly over the Indian Ocean and western Pacific. Specifically, strongly enhanced (suppressed) convection is generally preceded, both in time and space, by a low-level moist (dry) anomaly and followed by a low-level dry (moist)

anomaly (Figs. 7, 8, and 9). This is similar to the previous findings by Kemball-Cook and Weare (2001) based on radiosonde data, by Sperber (2003), Seo and Kim (2003), and Kiladis et al. (2005) based on NCEP or ECMWF and by Myers and Waliser (2003) based on TOVS. However, previous studies based on localized radiosonde data mainly focused on the temporal evolution (e.g., Kemball-Cook and Weare 2001), while those based on global reanalysis mainly focused on the spatial evolution (e.g., Sperber 2003; Kiladis et al. 2005). Here, we present a comprehensive spatial and temporal evolution of the MJO.

Comparison of Fig. 3 and Fig. 7 shows an interesting difference between the MJO vertical temperature and moisture structures. The preconditioning temperature anomaly is generally found in the lower troposphere (Fig. 3), while the preconditioning water vapor anomaly can reach up to the middle troposphere (around 500 hPa; Fig. 7). The preconditioning moist (dry) anomaly as exhibited by AIRS seems also to be divided into two steps. It first develops near the surface (below 925 hPa) under the region of strongly suppressed (enhanced) convection (Figs. 7 and 9). After about two pentads, the suppression (enhancement) of convection gets much weaker and the preconditioning water vapor anomaly reaches up to the middle troposphere (around 500 hPa). Then, after about 2 pentads, the suppressed (enhanced) convection vanishes and is replaced by enhanced (suppressed) convection (Figs. 7 and 8). For example, a moist anomaly can be clearly seen in the 648-hPa map (Fig. 8) over the equatorial Indian Ocean at lag −2 pentads and over the western Pacific at lag 0 pentads. This low-level moistening ahead of the MJO deep convection may be caused by the middle-level cumulus congestus clouds associated with shallow convection, which were observed during TOGA COARE (Johnson et al. 1999; Kikuchi and Takayabu 2004). Furthermore, combining deep convection and its associated preconditioning stage (i.e., weak and strongly suppressed convection) together, the trimodal vertical structure in the moisture anomaly from AIRS is clear, which seems to be consistent with the TOGA COARE soundings (Johnson et al. 1999; Kikuchi and Takayabu 2004).

4. Comparison of the MJO vertical structure between AIRS and NCEP

To better highlight the new results of the MJO vertical moist thermodynamic structure from AIRS and also to identify possible systematic errors in the NCEP reanalysis, we present a direct comparison of the MJO vertical moist thermodynamic structure based on AIRS with that from NCEP. Identical analysis and compositing procedures are applied to NCEP and AIRS, which are at the same period.

a. Comparison of the MJO vertical thermodynamic structure

A diagram similar to Fig. 3 but based on NCEP is shown in Fig. 10. Comparison between Figs. 3 and 10 suggests that both AIRS and NCEP show a similar temperature structure near the tropopause and in the free troposphere. For example, both data reveal a warm (cold) anomaly in the free troposphere and a cold (warm) anomaly near the tropopause collocated with enhanced (suppressed) convection, an eastward propagation of temperature anomalies with the convective anomaly, and a similar tilted temperature structure from west to east near the tropopause. However, the magnitude of the composite anomalies seems to be much larger in AIRS (±0.4 K) than NCEP (±0.2 K). Furthermore, the free-tropospheric warm (cold) anomaly center is typically collocated with the enhanced (suppressed) convection center in AIRS, but it shifts further eastward in NCEP.

Over the western Pacific, the lower-troposphere temperature anomaly has the same sign between AIRS and NCEP but the magnitude is much larger in AIRS than that in NCEP. Furthermore, the lower-troposphere temperature anomaly is more well-defined in AIRS than NCEP; that is, the transition from the lower-tropospheric warm (cold) anomaly to the free tropospheric cold (warm) anomaly is much sharper in AIRS than NCEP. In addition, the lower-troposphere temperature anomaly is much shallower in AIRS (below ~800 hPa) than NCEP (below ~700 hPa). These points are more clearly quantified in the upper panel of Fig. 11, which compares the area-averaged vertical profiles of the temperature anomaly difference between lag +4 pentads and lag 0 pentads (wet–dry conditions) over the equatorial western Pacific (8°S–8°N, 150°–160°E) based on AIRS and NCEP. The Student's *t* test also shows that the difference is statistically significant with 95% confidence level.

In addition, comparison of Figs. 3 and 10 illustrates even more significant differences in temperature anomaly between AIRS and NCEP exist in the lower-troposphere over the Indian Ocean where there are very few conventional data to constrain the reanalysis. Over the Indian Ocean, the well-defined lower-troposphere temperature anomaly (below 800 hPa) from AIRS (Fig. 3) is entirely different in NCEP (Fig. 10). AIRS suggests a bimodal structure in the troposphere; that is, positive (negative) in the free troposphere versus negative (positive) in the lower troposphere as well as a sharp transition between them, while

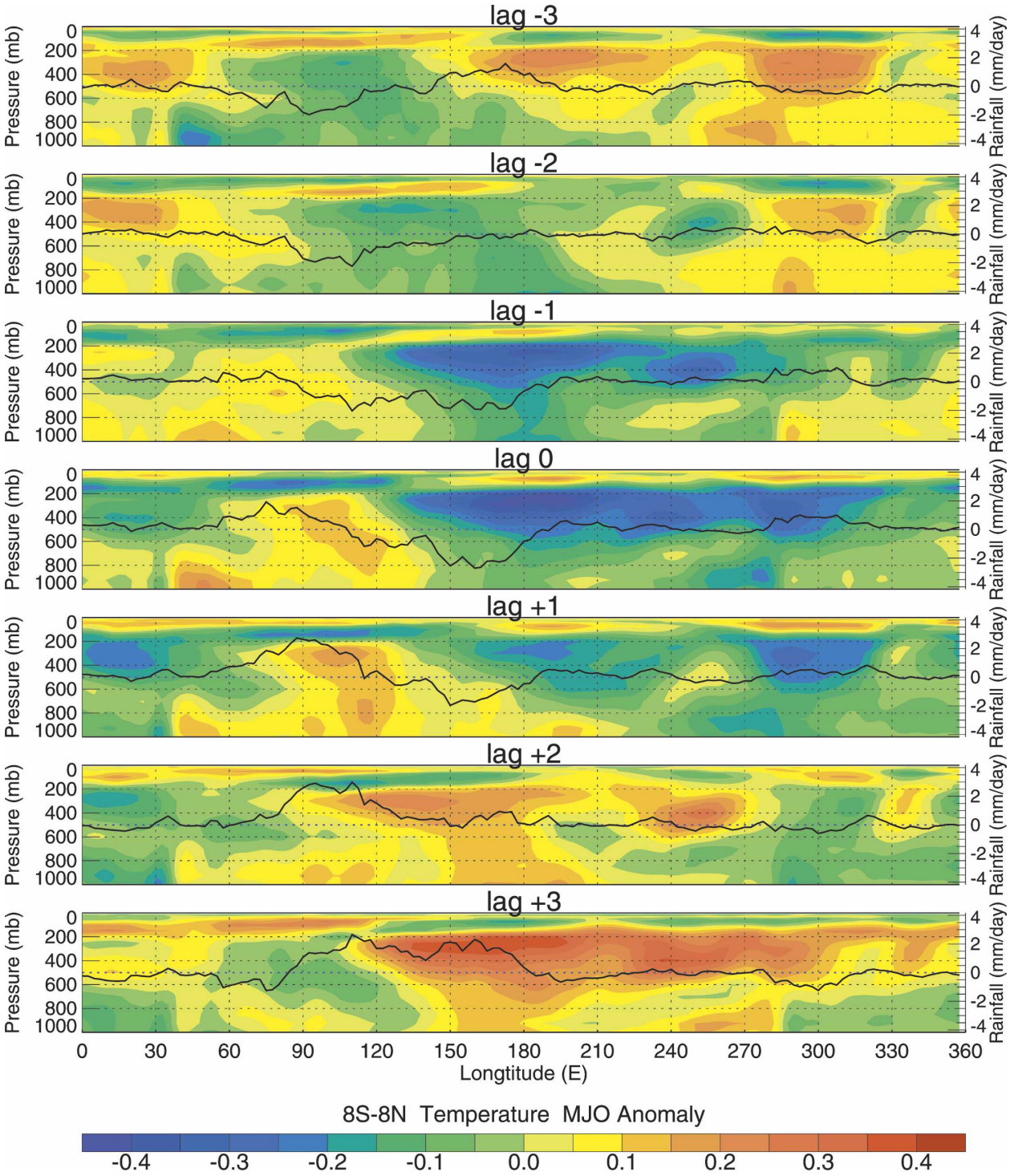

FIG. 10. As in Fig. 3 but based on NCEP. The superimposed solid black line also denotes the associated TRMM rainfall anomaly but at the NCEP spatial resolution (2.5° × 2.5°), which is smoother than that in Fig. 3. Considering the grid resolution, the latitude average extends between 8.75°S and 8.75°N.

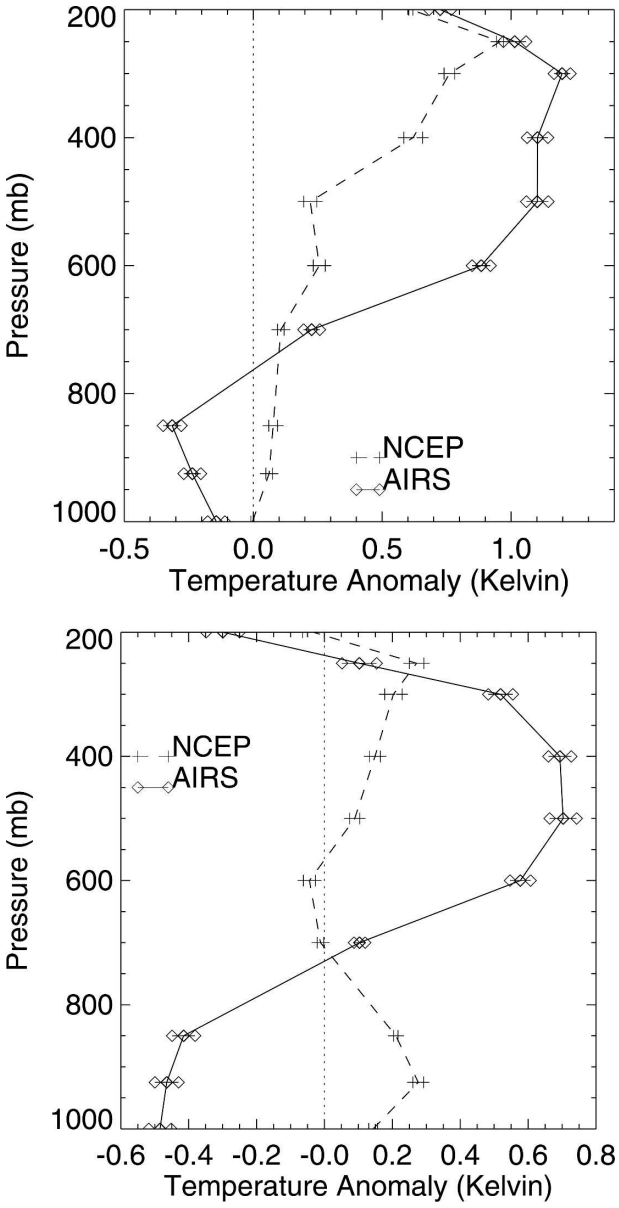

FIG. 11. Area-averaged vertical profiles of temperature anomaly (K) over the (top) equatorial western Pacific (8°S–8°N, 150°–160°E) and (bottom) the equatorial Indian Ocean (8°S–8°N, 90°–100°E) for AIRS (solid line) and NCEP (dashed line). To highlight the temperature signals, the difference between lag +4 pentads (wet phase) and lag 0 pentads (dry phase) for the western Pacific and the difference between lag +2 pentads and lag −2 pentads for the Indian Ocean are used. The error bar denotes the 95% confidence level within the domain.

the NCEP shows a constant-sign temperature anomaly throughout the troposphere for lags 0, ±4 pentads and the opposite sign anomalies for lags ±2 pentads. Furthermore, the signs of the lower-troposphere temperature anomaly are always opposite between AIRS and NCEP during nearly the whole course of the MJO cycle with negative (positive) anomalies for AIRS (Fig. 3), in contrast to positive (negative) in NCEP (Fig. 10), collocated with enhanced (suppressed) convection. This is illustrated more clearly in the lower panel of Fig. 11, which compares the area-averaged vertical profiles of the temperature anomaly difference between lag +2 pentads and lag −2 pentads over the equatorial Indian Ocean (8°S–8°N, 90°–100°E) based on AIRS and NCEP. It should be mentioned that a fundamental difference in the MJO vertical thermodynamic structure between AIRS and NCEP is that the AIRS-observed lower-troposphere preconditioning temperature anomaly over the Indian Ocean is absent in NCEP. This finding may have important implications for the MJO theory and is discussed in more detail in section 5.

b. Comparison of the MJO vertical moisture structure

The diagram similar to Fig. 7 but based on NCEP is shown in Fig. 12. Over the Eastern Hemisphere, especially the Indian Ocean, the propagation and vertical structure of the humidity anomaly in the troposphere above 900 hPa are roughly similar between AIRS and NCEP. For example, both datasets show that deep convection serves to locally moisten the upper troposphere (e.g., Held and Soden 2000; Tian et al. 2004). Both datasets also show a low-level moistening (drying) before the occurrence of strongly enhanced (suppressed) convection, similar to the findings by previous studies by Kemball-Cook and Weare (2001) based on radiosonde data, by Sperber (2003), Seo and Kim (2003), and Kiladis et al. (2005) based on NCEP or ECMWF and by Myers and Waliser (2003) based on TOVS. The overall magnitude of the tropospheric moist (dry) anomaly seems also to be roughly similar between AIRS and NCEP although regional differences are exhibited. As discussed in section 3b, the westward tilt of moisture anomaly with height in NCEP shown in Fig. 12 has been extensively documented by previous studies, such as Sperber (2003), Seo and Kim (2003), and Kiladis et al. (2005) based on NCEP or ECMWF and by Myers and Waliser (2003) based on TOVS and is also well reproduced by AIRS (Fig. 7).

However, there are a number of significant differences in the vertical moisture structures exhibited by AIRS and NCEP. To begin with, the NCEP water vapor is only available below 300 hPa, which is considered to be the maximum height of useful humidity data from reanalysis and radiosondes. Thus, any water vapor information above 300 hPa from AIRS could be considered as new compared with NCEP, although some caution is warranted as in overinterpreting the AIRS water

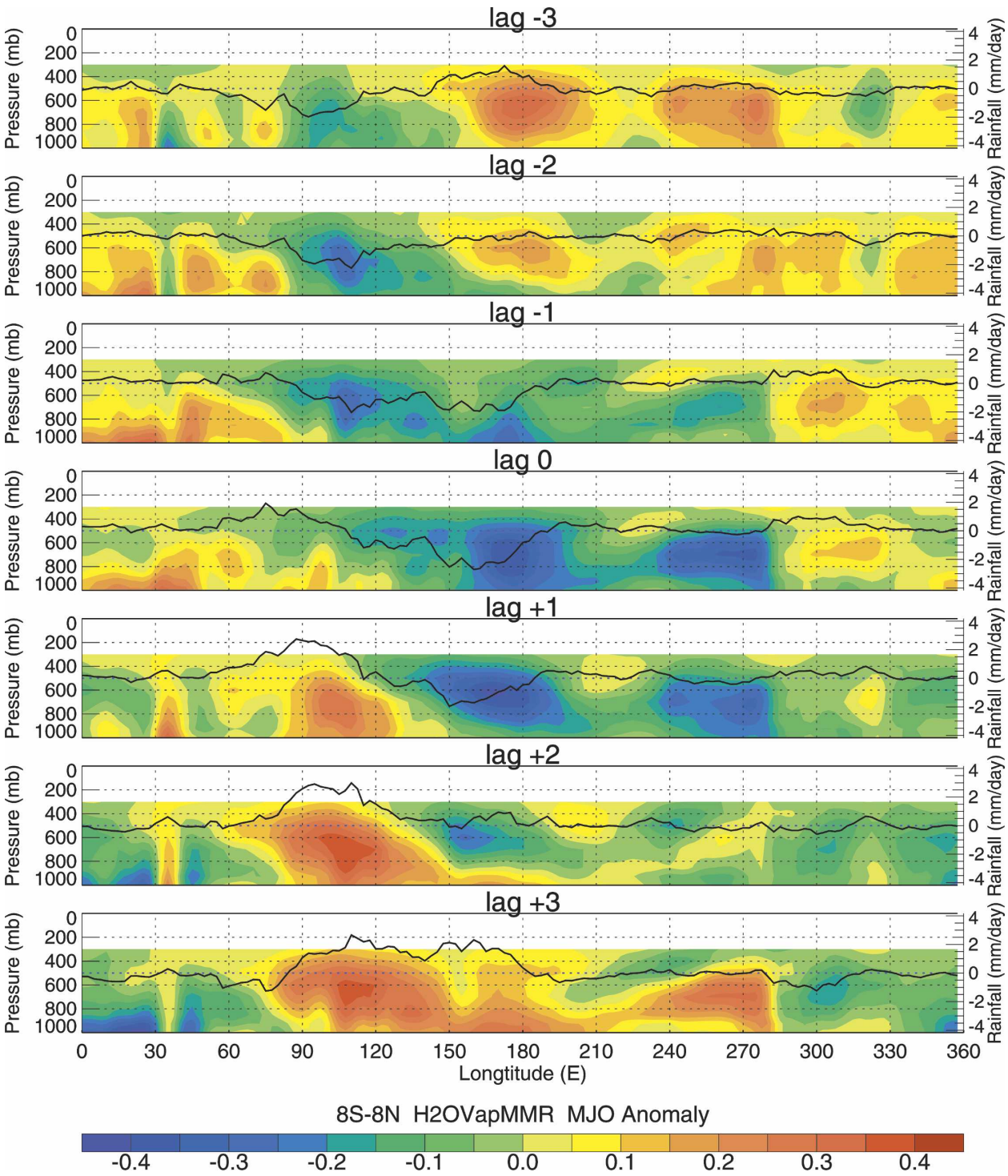

FIG. 12. As in Fig. 7 but based on NCEP.

vapor data above 150 hPa where it is known to begin to lose sensitivity.

Aside from the above issue, significant differences between AIRS and NCEP are found near the surface over the equatorial Indian Ocean and western Pacific. AIRS indicates a near-surface (below 925 hPa) preconditioning moist (dry) anomaly for enhanced (suppressed) convection under regions of strongly suppressed (enhanced) convection. For example, over the eastern Indian Ocean from ~90° to 120°E, there is a

clear near-surface moist (dry) anomaly at lag −2 pentads, which leads the enhanced convection at lag +2 pentad (Fig. 7). But this is absent in NCEP (Fig. 12). As a result, the near-surface water vapor anomaly under all regions of strong convection anomaly is nearly always opposite between AIRS and NCEP. In addition, closer inspection of the midtropospheric water vapor anomalies shows that the AIRS data appears to be more closely related to the TRMM rainfall anomalies than the NCEP. For example, in the Maritime Continent from ~120° to ~150°E, there is a local maximum in the rainfall anomaly at lag 0 pentads. Accordingly, a local maximum in the midtropospheric water vapor anomaly shows up nicely in AIRS but not in NCEP. This relation is further quantified in Fig. 13, which shows the scatterplot of the ~500-hPa water vapor anomaly versus the TRMM rainfall anomaly for the composite MJO cycle (lags 0, ±4 pentads) over the equatorial Indian Ocean and western Pacific (8°S–8°N, 50°–210°E). The upper figure based on AIRS clearly shows a strong positive correlation between the midtropospheric water vapor anomaly and the rainfall anomaly (with a correlation coefficient of around 0.86), while the bottom figure based on NCEP indicates the correlation is considerably weaker. Please note the data of AIRS, NCEP, and TRMM are all independent of each other.

Finally, a significant difference in the water vapor anomaly between AIRS (Fig. 7) and NCEP (Fig. 12) can be found in the central Pacific. For example, NCEP shows a relatively uniform water vapor anomaly across the Pacific from the western Pacific to the eastern Pacific with a weakened amplitude in the central Pacific (around 180°–210°E). However, AIRS indicates an anomaly of the opposite sign over the central Pacific compared to the values to its east and west. AIRS also suggests nearly vertically uniform moist anomalies over the western Pacific and even an eastward tilt of moisture anomalies with height over the central Pacific around 150°W (Myers and Waliser 2003, see their Fig. 12), a feature that is considerably less obvious in NCEP.

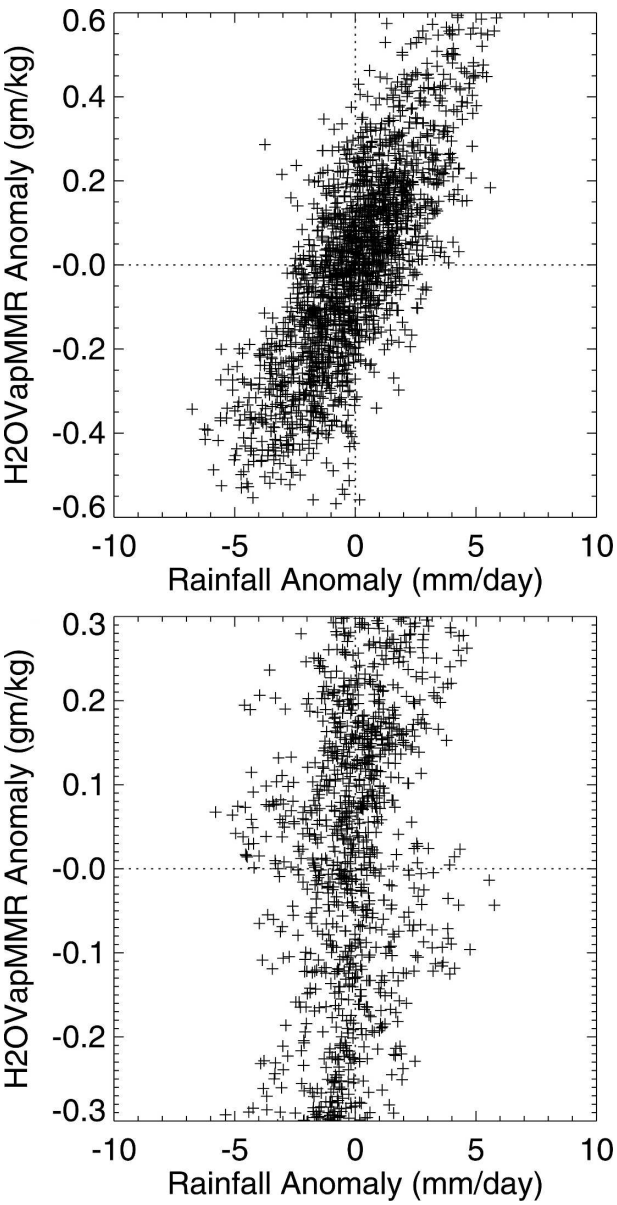

FIG. 13. The midtropospheric specific humidity anomaly vs the TRMM rainfall anomaly for the composite MJO cycle (lags 0, ±4 pentads) over the equatorial Indian Ocean and western Pacific (8°S–8°N, 50°–210°E) between (top) AIRS (547 hPa) and (bottom) NCEP (500 hPa).

c. Discussion

The comparison in the vertical moist thermodynamic structure between AIRS and NCEP in the last two subsections shows broad agreement in their representation of the MJO. However, it also illustrates a number of striking differences, especially in the lower troposphere over the Indian Ocean and over the central and eastern Pacific Ocean. These differences are statistically large and occur in regions that are important for model and theory validation. To explore the reasons for these differences, a number of additional sensitivity analyses were performed. Comparison of the MJO vertical structure based on the twice-daily NCEP data (0000 and 1200 UTC or 0600 and 1800 UTC) and that from the 4-time daily NCEP data demonstrated (not shown) that these diurnal sampling differences did not qualitatively influence the depiction of the MJO cycle. This is an indication that the differences exhibited between AIRS and NCEP are not due to the sampling issues (twice-daily satellite sampling for AIRS and 4-time daily synoptic sampling for NCEP). Comparison of the

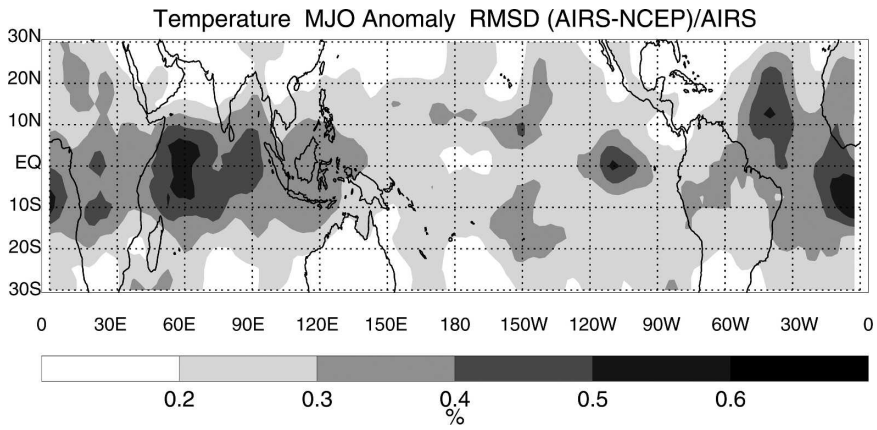

FIG. 14. Temperature anomaly root-mean-square difference (RMSD) between AIRS and NCEP.

MJO vertical structure between NCEP and NCEP2[1] (not shown) shows that their overall MJO vertical structure is very similar, thus implying that the differences between AIRS and NCEP2 are qualitatively the same as those discussed above between AIRS and NCEP.

Given the significant differences between AIRS and NCEP discussed above, it is worthwhile to consider the general shortcomings of each dataset in trying to understand their differences. In the case of AIRS data, it is well known that the infrared and microwave based remote sensing techniques are still a developing field and thus subject to considerable uncertainties, especially in the region of intense cloud cover and heavy precipitation and also in the lower troposphere (Susskind et al. 2003; Fetzer et al. 2006). For example, where MJO convection is active, the AIRS full retrieval yield can be as low as 10% and this low yield would propagate eastward in accordance with the MJO itself. Nevertheless, Fetzer et al. (2006) have shown that the sampling biases of the total precipitable water vapor in these deep convective regions are small compared with the Advanced Microwave Sounding Radiometer for Earth Observing Satellite (EOS; AMSR-E). However, the height-dependent biases in temperature and water vapor profiles have yet to be quantified.

In the case of the reanalysis, such as NCEP or NCEP2, the scarcity of radiosonde and other conventional data over the tropical oceans is an important consideration. For example, over the Indian Ocean, part of the western Pacific and most of the central and eastern Pacific there is very little radiosonde data to constrain the analysis. Thus, the reanalysis over these regions are mostly model-driven and may contain large errors from the model's boundary layer, deep convection, and cloud parameterizations. Along these lines, it is interesting to note that the comparisons in section 4a showed that the temperature anomaly difference between AIRS and NCEP is larger over the data-sparse Indian Ocean than that over the western Pacific. To more succinctly quantify this point, the root-mean-square (RMS) difference of temperature anomaly between AIRS and NCEP is shown in Fig. 14. For this figure, the RMS difference was calculated over the 11-pentad cycle, normalized by the standard deviation of the AIRS temperature anomaly, and then vertically averaged from 200 to 1000 hPa. Clearly, the RMS difference is higher over radiosonde-sparse regions, particularly the Indian Ocean and to some extent the eastern Pacific and Atlantic Oceans. This may partially validate our speculation above concerning model-driven errors in the reanalysis. It should be noted that climate models have a notoriously difficult time representing the MJO over the Indian Ocean, which is also consistent with our above speculation.

While the above comparison raises concerns about NCEP it does not provide validation for the AIRS profiles of MJO temperature structure. Along with the previous mentioned AIRS validations studies (i.e., Gettelman et al. 2004; Divakarla et al. 2006; Tobin et al. 2006), Fig. 15 illustrates a comparison between AIRS and radiosonde data at Truk to check the reliability of the AIRS data in the context of the MJO. This figure shows there is relatively good agreement between AIRS and radiosonde temperature profiles at this location over the life cycle of the MJO. The reduced coherence of the radiosonde stratospheric temperature structure may be due to the smaller sampling of radiosonde above 100 hPa. The reduced coherence of the AIRS upper tropo-

[1] Only seven MJO events were included in the composite MJO cycle for NCEP2 instead of eight MJO events using AIRS and NCEP because the NCEP2 data period does not include 2005.

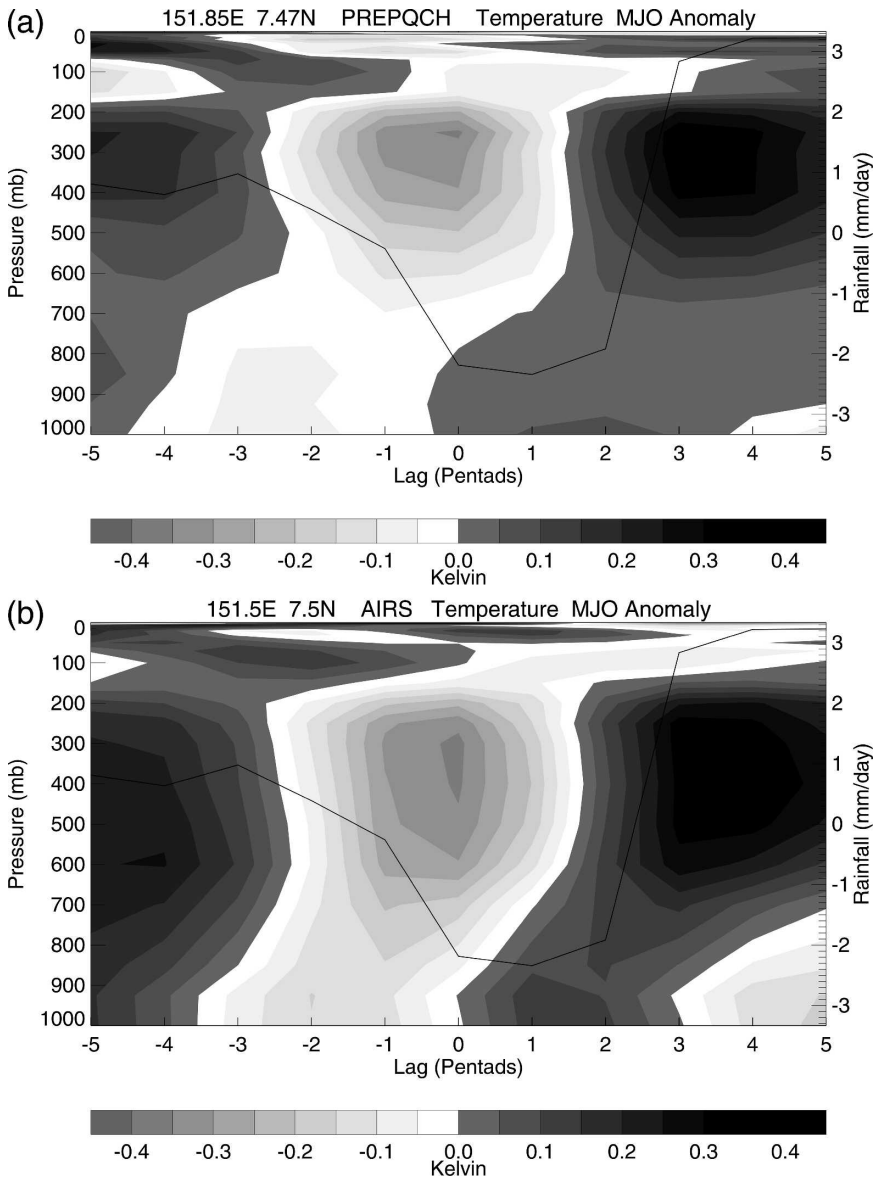

FIG. 15. MJO vertical temperature structure using (top) radiosonde and (bottom) AIRS at Truk (7.47°N, 151.85°E). The superimposed solid black line denotes the collocated TRMM rainfall anomaly (mm day^{-1}).

spheric temperatures may be due to decreasing AIRS vertical resolution with altitude (Aumann et al. 2003). While the agreement is not perfect, uncertainties associated with the differences in the spatial scale of the two measurement techniques, and the influence of land–sea contrast on each of these, as well as AIRS retrieval errors, all also likely contribute to the differences.

The scatter diagrams between midtroposphere water vapor anomalies and TRMM rainfall anomalies in Fig. 16 elicit similar concerns and findings regarding NCEP water vapor anomalies and also support the above speculation concerning the impact of data sparse regions on the reanalysis. These diagrams are analogous to Fig. 13 but using only the subset of points from the Indian Ocean domain. The contrast between AIRS and NCEP is even more dramatic when considering the Indian Ocean alone, with the indication that AIRS is better capturing the expected positive relation between rainfall and midtropospheric water vapor anomalies.

5. Summary and discussion

In this study, the high-resolution temperature and water vapor soundings from AIRS are used to characterize the vertical moist thermodynamic structure and

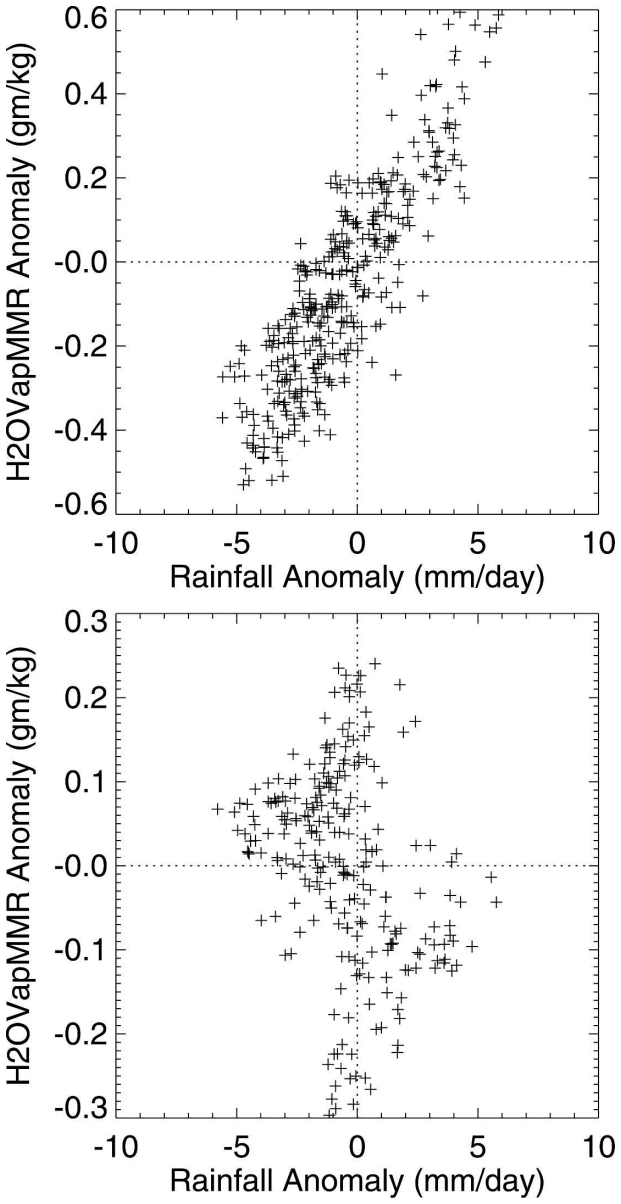

FIG. 16. As in Fig. 13 but for the equatorial Indian Ocean (8°S–8°N, 70°–100°E) only.

spatial–temporal evolution of the MJO. The AIRS data have revealed a coherent spatial and temporal relationship between deep convection and atmospheric vertical moist thermodynamic structure associated with the MJO.

In the Indian Ocean and western Pacific, the AIRS temperature anomaly shows a trimodal vertical structure: a warm (cold) anomaly in the free troposphere (800–250 hPa) and a cold (warm) anomaly near the tropopause (above 250 hPa) and in the lower troposphere (below 800 hPa) associated with enhanced (suppressed) convection (Figs. 3, 4, 5, and 6). Over the Western Hemisphere, a bimodal vertical structure typically exists in the AIRS temperature anomaly with troposphere and stratosphere anomalies being out of phase and with the tropospheric anomalies appearing to emanate from, and thus have the same sign as, those over the western Pacific (Figs. 3, 4, 5, and 6).

The AIRS moisture anomaly shows markedly different vertical structures as a function of longitude and the strength of convection anomaly (Figs. 7, 8, and 9). In the region of strongly enhanced (suppressed) convection, moist (dry) anomalies are generally found throughout the atmospheric column except for weak dry (moist) anomalies near the surface (961 hPa). In the region of weakly enhanced (suppressed) convection, moist (dry) anomalies are usually found in the upper troposphere (above 500 hPa) and opposite anomalies in the lower troposphere (below 500 hPa). AIRS also shows a westward tilt of moisture anomalies with height over the Indian Ocean, nearly vertically uniform moist anomalies over the western Pacific, and an eastward tilt of moisture anomalies with height over the central Pacific (Fig. 7). In the eastern Pacific, the water vapor anomalies are surprisingly large and mainly confined to the lower troposphere (below 500 hPa; Fig. 7).

Comparisons of the MJO vertical temperature structure between AIRS and NCEP suggest that both AIRS and NCEP show a similar temperature structure near the tropopause and, to a large extent, in the free troposphere (Figs. 3 and 10). However, significant lower-troposphere temperature differences exist over western Pacific and the Indian Ocean. The anomalous lower-troposphere temperature structure is much less well defined in NCEP than in AIRS for the western Pacific, and even has the opposite sign anomalies compared to AIRS relative to the wet/dry phase of the MJO in the Indian Ocean (Figs. 3, 10, and 11). Both AIRS and NCEP also show a roughly similar propagation and vertical structure of the humidity anomaly in the troposphere above 900 hPa over the Eastern Hemisphere (Figs. 7, 8, 9, and 12). However, significant differences are found for the near-surface and midtropospheric humidity anomalies over the equatorial Indian Ocean (Figs. 7, 12, 13, and 16) and moist vertical structure over the western and central Pacific. It is suggested that the model-driven errors such as parameterization deficiencies in the reanalysis may contribute to these differences between AIRS and NCEP.

Most significantly, the AIRS data demonstrate that there exists a clear lower-troposphere moist thermodynamic structure over the Indian Ocean and western Pacific, that is, the enhanced (suppressed) convection is generally preceded by a lower-tropospheric warm and moist (cold and dry) anomaly about 3 pentads earlier or around 60° to the east and followed by a lower-tropospheric cold and dry (warm and moist) anomaly

after or under and to the west (Figs. 3 and 7). But this low-level moist thermodynamic preconditioning, especially the low-level warming and cooling, is not well reproduced by NCEP.

The vertical moist thermodynamic structure in AIRS observations may have important implications for our theoretical understanding of the MJO. First, the low-level moist thermodynamic preconditioning can hardly be explained by thermodynamic theories alone. The thermodynamic theories such as cloud–radiation feedback (Hu and Randall 1994; Raymond 2001) and discharge–recharge (Blade and Hartmann 1993; Kemball-Cook and Weare 2001), or convection–moisture feedback (Woolnough et al. 2000; Tompkins 2001) only produce stationary oscillation. On the other hand, the low-level preconditioning structure can be explained by the frictional Kelvin–Rossby wave–conditional instability of the second kind (CISK) model.

Equatorial wave dynamics (Matsuno 1966; Gill 1980) have been regarded as a cornerstone to understanding equatorial large-scale circulations and its variabilities. In the frictional Kelvin–Rossby wave–CISK theory for the MJO (Wang 1988, 2005; Wang and Rui 1990b; Wang and Li 1994; Salby et al. 1994), the nonlinear interactions among convective-condensational heating, low-frequency equatorial (Rossby and Kelvin) waves, boundary layer moist dynamics, and wind-induced heat exchange at the surface are fundamental physical components of this MJO theory. Given an initial heating centered on the equator, the theory predicts easterlies (westerlies) to the east of (west of and under) the heating as a baroclinic Kelvin (Rossby) wave response. Geostrophic balance in equatorial zonal winds requires that inviscid low-level easterly wind perturbations be accompanied by a pressure trough at the equator, whereas low-level westerlies should be accompanied by a pressure maximum at the equator. Therefore, friction would foster mass convergence into the equatorial pressure trough in the easterly regime and mass divergence into the equatorial pressure maximum in the westerlies (Wang and Rui 1990b). This lead/lag relationship between the surface convergence and MJO deep convection (Fig. 10.13 of Wang 2005) has been well documented by observational studies, such as Rui and Wang (1990), Hendon and Salby (1994), Zhang (1996), Jones and Weare (1996), Maloney and Hartmann (1998), Matthews (2000), Seo and Kim (2003), Sperber (2003), and Kiladis et al. (2005). The surface frictional mass convergence associated with equatorial Kelvin waves should result in low-level moistening and warming ahead of the convection, while the surface frictional mass divergence associated with equatorial Rossby waves should result in low-level drying and cooling behind and under the convection. The low-level moist thermodynamic preconditioning structure observed from AIRS is consistent with this theoretical prediction. Also as discussed in section 3, the significant equatorial 100- and 400-hPa temperature anomalies over the central and eastern Pacific as well as the significant off-equatorial 100- and 400-hPa temperature anomalies over the Eastern Hemisphere (Figs. 3, 4, and 5) imply an equatorial Kelvin–Rossby wave response to MJO convection, which are also consistent with the frictional wave–CISK model.

A number of diagnostic studies of the model simulations have also confirmed the importance of the boundary layer frictional convergence/divergence in model-simulated MJO variability in a number of climate models with different cumulus parameterization schemes (e.g., Lau and Lau 1986; Lau et al. 1988; Maloney 2002; Lee et al. 2003; Liu et al. 2005) and in a coupled climate model (Waliser et al. 1999). Although the simplistic two and a half layer frictional feedback model cannot describe the multiple time and spatial scales involved in MJO and its simple representation of diabatic heating presumes direct coupling between the MJO disturbance and convection, the model results suggest that to simulate the MJO realistically, the cumulus parameterization scheme has to allow the large-scale low-frequency waves and associated boundary layer dynamics to feel the effects of the parameterized convective heating and to have some effects on the parameterized heating either directly or indirectly. Based on the evaluation of MJO simulations in 14 coupled GCMs participating in the Intergovernmental Panel on Climate Change (IPCC) Fourth Assessment Report (AR4), Lin et al. (2006) found that the two models that arguably do best at simulating the MJO are the only ones having convective closures/triggers linked in some way to moisture convergence. This lends further support to the relevance of the frictional Kelvin–Rossby wave–CISK theory.

However, it should be noted that many other factors may be at work as well. For example, the near-surface cooling and drying may indicate the influence of enhanced or suppressed convective downdrafts on the boundary layer (Fu et al. 2006). It is also possible that the intraseasonal sea surface temperature (SST) anomalies may contribute to the low-level moist thermodynamic preconditioning by enhancing turbulent surface fluxes or low-level meridional convergence associated with the frictional wave–CISK (Shinoda et al. 1998; Waliser et al. 1999; Fu et al. 2006). To fully understand this issue, detailed energy and moisture budget studies based on high-quality data of boundary layer wind, SST, and surface heat fluxes are needed.

Acknowledgments. This work was supported by the AIRS project at Jet Propulsion Laboratory (JPL) and JPL's Research and Technology Development program. In addition, the second author was supported by JPL's Human Resources Development fund. The research at JPL, California Institute of Technology was performed under contracts with the National Aeronautics and Space Administration. The AIRS level 3 data as well as the NCEP PREPQC radiosonde data were provided by Stephanie Granger, Ed Olsen, and Sung-Yung Lee, who also provided assistance in the analysis. The TRMM 3B42 rainfall data were downloaded from GSFC DAAC web site. The NCEP and NCEP2 reanalysis data were provided by the NOAA–CIRES Climate Diagnostics Center, Boulder, Colorado, from their Web site. Insightful reviews and constructive comments from George Kiladis and two anonymous reviewers as well as helpful discussions with Mous Chahine, Evan Fishbein, Xiouhua Fu, William Lau, and Ken Sperber are appreciated. The first author also wants to thank Mike Black and Xun Jiang for programming help.

REFERENCES

Aumann, H. H., and Coauthors, 2003: AIRS/AMSU/HSB on the Aqua Mission: Design, science objectives, data products, and processing systems. *IEEE Trans. Geosci. Remote Sens.,* **41,** 253–264.

Bantzer, H., and J. M. Wallace, 1996: Intraseasonal variability in tropical-mean temperature and precipitation and their relation to the tropical 40–50-day oscillation. *J. Atmos. Sci.,* **53,** 3042–3045.

Blade, I., and D. L. Hartmann, 1993: Tropical intraseasonal oscillations in a simple nonlinear model. *J. Atmos. Sci.,* **50,** 2922–2939.

Chahine, M. T., 1968: Determination of the temperature profile in the atmosphere from its outgoing radiance. *J. Opt. Soc. Amer.,* **58,** 1634–1637.

——, 1977: Remote sounding in cloudy atmospheres. II. Multiple cloud formations. *J. Atmos. Sci.,* **34,** 744–757.

Divakarla, G. D., C. D. Barnet, M. D. Goldberg, L. M. McMillin, E. Maddy, W. Wolf, L. Zhou, and X. Liu, 2006: Validation of Atmospheric Infrared Sounder temperature and water vapor retrievals with matched radiosonde measurements and forecasts. *J. Geophys. Res.,* **111,** D09S15, doi:10.1029/2005JD006116.

Eguchi, N., and M. Shiotani, 2004: Intraseasonal variations of water vapor and cirrus clouds in the tropical upper troposphere. *J. Geophys. Res.,* **109,** D12106, doi:10.1029/2003JD004314.

Fetzer, E. J., B. H. Lambrigtsen, A. Eldering, H. H. Aumann, and M. T. Chahine, 2006: Biases in total precipitable water vapor climatologies from Atmospheric Infrared Sounder and Advanced Microwave Scanning Radiometer. *J. Geophys. Res.,* **111,** D09S16, doi:10.1029/2005JD006598.

Fu, X., B. Wang, and L. Tao, 2006: Satellite data reveal the 3-D moisture structure of tropical intraseasonal oscillation and its coupling with underlying ocean. *Geophys. Res. Lett.,* **33,** L03705, doi:10.1029/2005GL025074.

Gettelman, A., and Coauthors, 2004: Validation of Aqua satellite data in the upper troposphere and lower stratosphere with in situ aircraft instruments. *Geophys. Res. Lett.,* **31,** L22107, doi:10.1029/2004GL020730.

Gibson, J. K., P. Kallberg, S. Uppala, A. Hernandez, A. Nomura, and E. Serrano, 1997: ERA description. ECMWF Re-Analysis Project Rep. Series 1, European Centre for Medium-Range Weather Forecasts, 72 pp.

Gill, A. E., 1980: Some simple solutions for heat-induced tropical circulation. *Quart. J. Roy. Meteor. Soc.,* **106,** 447–462.

Held, I. M., and B. J. Soden, 2000: Water vapor feedback and global warming. *Annu. Rev. Energy Environ.,* **25,** 441–475.

Hendon, H. H., and B. Liebmann, 1990: The intraseasonal (30–50 day) oscillation of the Australian summer monsoon. *J. Atmos. Sci.,* **47,** 2909–2923.

——, and M. L. Salby, 1994: The life cycle of the Madden–Julian oscillation. *J. Atmos. Sci.,* **51,** 2225–2237.

Hsu, H.-H., and M.-Y. Lee, 2005: Topographic effects on the eastward propagation and initiation of the Madden–Julian oscillation. *J. Climate,* **18,** 795–809.

Hu, Q., and D. A. Randall, 1994: Low-frequency oscillations in radiative-convective systems. *J. Atmos. Sci.,* **51,** 1089–1099.

Johnson, R. H., T. M. Rickenbach, S. A. Rutledge, P. E. Ciesielski, and W. H. Schubert, 1999: Trimodal characteristics of tropical convection. *J. Climate,* **12,** 2397–2418.

Jones, C., and B. C. Weare, 1996: The role of low-level moisture convergence and ocean latent heat fluxes in the Madden and Julian oscillation: An observational analysis using ISCCP data and ECMWF analyses. *J. Climate,* **9,** 3086–3104.

——, L. M. V. Carvalho, R. W. Higgins, D. E. Waliser, and J.-K. E. Schemm, 2004: Climatology of tropical intraseasonal convective anomalies: 1979–2002. *J. Climate,* **17,** 523–539.

Kalnay, E., and Coauthors, 1996: The NCEP/NCAR 40-Year Reanalysis Project. *Bull. Amer. Meteor. Soc.,* **77,** 437–471.

Kanamitsu, M., W. Ebisuzaki, J. Woollen, S.-K. Yang, J. J. Hnilo, M. Fiorino, and G. L. Potter, 2002: NCEP-DOE AMIP-II Reanalysis (R-2). *Bull. Amer. Meteor. Soc.,* **83,** 1631–1643.

Kemball-Cook, S. R., and B. C. Weare, 2001: The onset of convection in the Madden–Julian oscillation. *J. Climate,* **14,** 780–793.

Kikuchi, K., and Y. N. Takayabu, 2004: The development of organized convection associated with the MJO during TOGA COARE IOP: Trimodal characteristics. *Geophys. Res. Lett.,* **31,** L10101, doi:10.1029/2004GL019601.

Kiladis, G. N., K. H. Straub, and P. T. Haertel, 2005: Zonal and vertical structure of the Madden–Julian oscillation. *J. Atmos. Sci.,* **62,** 2790–2809.

Kim, H., and A. E. Dessler, 2004: Observations of convective cooling in the tropical tropopause layer in AIRS data. *Atmos. Chem. Phys. Discuss.,* **4,** 7615–7629.

Lau, K.-M., and D. E. Waliser, 2005: *Intraseasonal Variability in the Atmosphere-Ocean Climate System*. Springer Praxis Books, 474 pp.

Lau, N.-C., and K. M. Lau, 1986: Structure and propagation of intraseasonal oscillations appearing in a GFDL GCM. *J. Atmos. Sci.,* **43,** 2023–2047.

——, I. M. Held, and J. D. Neelin, 1988: The Madden–Julian oscillation in an idealized general circulation model. *J. Atmos. Sci.,* **45,** 3810–3832.

Lee, M. I., I. S. Kang, and B. E. Mapes, 2003: Impacts of cumulus convection parameterization on aqua-planet AGCM simulations of tropical intraseasonal variability. *J. Meteor. Soc. Japan,* **81,** 963–992.

Lin, J. L., and Coauthors, 2006: Tropical intraseasonal variability in 14 IPCC AR4 climate models. Part I: Convective signals. *J. Climate,* **19,** 2665–2690.

Lin, X., and R. H. Johnson, 1996: Kinematic and thermodynamic characteristics of the flow over the western Pacific warm pool during TOGA/COARE. *J. Atmos. Sci.,* **53,** 695–715.

Liu, P., B. Wang, K. Sperber, T. Li, and G. A. Meehl, 2005: MJO in CAM2 with Tiedtke convective scheme. *J. Climate,* **18,** 3007–3020.

Madden, R., 1986: Seasonal variations of the 40–50-day oscillation in the tropics. *J. Atmos. Sci.,* **43,** 3138–3158.

——, and P. R. Julian, 1971: Description of a 40-50 day oscillation in the zonal wind in the tropical Pacific. *J. Atmos. Sci.,* **28,** 1109–1123.

——, and ——, 1972: Description of global scale circulation cells in the tropics with a 40-50 day period. *J. Atmos. Sci.,* **29,** 1109–1123.

——, and ——, 2005: Historical perspective. *Intraseasonal Variability in the Atmosphere–Ocean Climate System,* K. M. Lau and D. E. Waliser, Eds., Praxis, 1–18.

Maloney, E. D., 2002: An intraseasonal oscillation composite life cycle in the CCM3.6 with modified convection. *J. Climate,* **15,** 964–982.

——, and D. L. Hartmann, 1998: Frictional moisture convergence in a composite life cycle of the Madden–Julian oscillation. *J. Climate,* **11,** 2387–2403.

Matsuno, T., 1966: Quasigeostrophic motions in the equatorial area. *J. Meteor. Soc. Japan,* **44,** 25–43.

Matthews, A. J., 2000: Propagation mechanisms for the Madden-Julian Oscillation. *Quart. J. Roy. Meteor. Soc.,* **126,** 2637–2652.

Myers, D., and D. E. Waliser: 2003: Three-dimensional water vapor and cloud variations associated with the Madden–Julian oscillation during Northern Hemisphere winter. *J. Climate,* **16,** 929–950.

Parkinson, C. L., 2003: Aqua: an Earth-Observing Satellite mission to examine water and other climate variables. *IEEE Trans. Geosci. Remote Sens.,* **41,** 173–183.

Raymond, D. J., 2001: A new model of the Madden–Julian oscillation. *J. Atmos. Sci.,* **58,** 2807–2819.

Rosenkranz, P. W., 2003: Rapid radiative transfer model for AMSU/HSB channels. *IEEE Trans. Geosci. Remote Sens.,* **41,** 362–368.

Rui, H., and B. Wang, 1990: Development characteristics and dynamical structure of tropical intraseasonal convection anomalies. *J. Atmos. Sci.,* **47,** 357–379.

Salby, M. L., R. R. Garcia, and H. H. Hendon, 1994: Planetary-scale circulations in the presence of climatological and wave-induced heating. *J. Atmos. Sci.,* **51,** 2344–2367.

Seo, K.-H., and K.-Y. Kim, 2003: Propagation and initiation mechanisms of the Madden-Julian oscillation. *J. Geophys. Res.,* **108,** 4384, doi:10.1029/2002JD002876.

Sherwood, S. C., and A. E. Dessler, 2000: On the control of stratospheric humidity. *Geophys. Res. Lett.,* **27,** 2513–2516.

——, T. Horinouchi, and H. A. Zeleznik, 2003: Convective impact on temperatures observed near the tropical tropopause. *J. Atmos. Sci.,* **60,** 1847–1856.

Shinoda, T., H. H. Hendon, and J. Glick, 1998: Intraseasonal variability of surface fluxes and sea surface temperature in the tropical western Pacific and Indian Oceans. *J. Climate,* **11,** 1685–1702.

Slingo, J. M., 2005: Modeling. *Intraseasonal Variability in the Atmosphere–Ocean Climate System,* K. M. Lau and D. E. Waliser, Eds., Praxis, 361–388.

Slingo, J. M., and Coauthors, 1996: Intraseasonal oscillations in 15 atmospheric general circulation models: Results from an AMIP diagnostic subproject. *Climate Dyn.,* **12,** 325–357.

——, P. M. Inness, and K. R. Sperber, 2005: Modeling. *Intraseasonal Variability in the Atmosphere–Ocean Climate System,* K. M. Lau and D. E. Waliser, Eds., Praxis, 361–388.

Sperber, K. R., 2003: Propagation and the vertical structure of the Madden–Julian oscillation. *Mon. Wea. Rev.,* **131,** 3018–3037.

Strow, L. L., S. E. Hannon, S. De Souza-Machado, H. E. Motteler, and D. Tobin, 2003: An overview of the AIRS radiative transfer model. *IEEE Trans. Geosci. Remote Sens.,* **41,** 390–409.

Susskind, J., C. Barnet, and J. Blaisdell, 2003: Retrieval of atmospheric and surface parameters from AIRS/AMSU/HSB data in the presence of clouds. *IEEE Trans. Geosci. Remote Sens.,* **41,** 390–409.

Tian, B., B. J. Soden, and X. Wu, 2004: Diurnal cycle of convection, clouds, and water vapor in the tropical upper troposphere: Satellites versus a general circulation model. *J. Geophys. Res.,* **109,** D10101, doi:10.1029/2003JD004117.

Tobin, D. C., and Coauthors, 2006: Atmospheric Radiation Measurement site atmospheric state best estimates for Atmospheric Infrared Sounder temperature and water vapor retrieval validation. *J. Geophys. Res.,* **111,** D09S14, doi:10.1029/2005JD006103.

Tompkins, A. M., 2001: On the relationship between tropical convection and sea surface temperature. *J. Atmos. Sci.,* **58,** 529–545.

Waliser, D. E., 2006: Predictability of tropical intraseasonal variability. *Predictability of Weather and Climate,* T. N. Palmer and R. Hagedorn, Eds., Cambridge University Press, 718 pp.

——, K. M. Lau, and J. H. Kim, 1999: The influence of coupled sea surface temperatures on the Madden–Julian oscillation: A model perturbation experiment. *J. Atmos. Sci.,* **56,** 333–358.

——, ——, W. Stern, and C. Jones, 2003a: Potential predictability of the Madden–Julian oscillation. *Bull. Amer. Meteor. Soc.,* **84,** 33–50.

——, and Coauthors, 2003b: AGCM simulations of intraseasonal variability associated with the Asian summer monsoon. *Climate Dyn.,* **21,** 423–446.

Wang, B., 1988: Dynamics of tropical low-frequency waves: An analysis of the moist Kelvin wave. *J. Atmos. Sci.,* **45,** 2051–2065.

——, 2005: Theories. *Intraseasonal Variability in the Atmosphere–Ocean Climate System,* K. M. Lau and D. E. Waliser, Eds., Praxis, 307–360.

——, and J.-K. Chen, 1989: On the zonal-scale selection and vertical structure of equatorial intraseasonal waves. *Quart. J. Roy. Meteor. Soc.,* **115,** 1301–1323.

——, and H. Rui, 1990a: Synoptic climatology of transient tropical intraseasonal convection anomalies. *Meteor. Atmos. Phys.,* **44,** 43–61.

——, and ——, 1990b: Dynamics of the coupled moist Kelvin–Rossby wave on an equatorial beta plane. *J. Atmos. Sci.,* **47,** 397–413.

——, and T. Li, 1994: Convective interaction with boundary-layer dynamics in the development of a tropical intraseasonal system. *J. Atmos. Sci.,* **51,** 1386–1400.

Weare, B. C., and J. S. Nasstrom, 1982: Examples of extended empirical orthogonal function analyses. *Mon. Wea. Rev.,* **110,** 481–485.

Woolnough, S. J., J. M. Slingo, and B. J. Hoskins, 2000: The relationship between convection and sea surface temperature on intraseasonal time scales. *J. Climate,* **13,** 2086–2104.

Zhang, C., 1996: Atmospheric intraseasonal variability at the surface in the tropical western Pacific ocean. *J. Atmos. Sci.,* **53,** 739–758.

——, 2005: Madden–Julian oscillation. *Rev. Geophys.,* **43,** RG2003, doi:10.1029/2004RG000158.

——, and M. Dong, 2004: Seasonality of the MJO. *J. Climate,* **17,** 3169–3180.